CHAPTER-6

Amorphous/crystalline interfaces in amorphous-steel coatings and nanocomposites

Chapter 6.
Amorphous/crystalline interfaces in amorphous steel coatings and nanocomposites

6.1 Introduction

Iron-based bulk amorphous alloys heralded a new era owing to their optimum blend of physical, chemical, mechanical and functional properties. They could be exploited for different technological applications [198,329]. Bulk Amorphous Steels (BAS) can overcome the dimensional limitations encountered in rapidly solidified iron-based metallic glasses. In addition to the increased thickness, BAS also exhibits enhanced corrosion resistance, mechanical strength, better fracture toughness, etc. [209,212,330–333]. They may find application in semiconductor, electronics and packaging industries, aerospace, power sector, healthcare sector, consumer appliance, transportation and renewable energy etc. [207,334,335]. Owing to the limitation of ductility of BAS or other bulk metallic glasses, the researchers have been trying to optimize the microstructure through the design of nanocomposites to achieve an optimum combination of properties [201,207,336–339]. Microstructural characteristics pertaining to the shape, size, structure and volume fraction of the dispersed phases can be tailored to optimize the properties like specific strength, ductility, fracture toughness etc. [207,340–342].

Fe-based amorphous alloys or BASs are different from other bulk metallic glasses (BMGs). BASs always have metal-metalloid combinations in them. Initial years, after discovery of this class of glass forming alloy system, had seen a resurgence in discovering new alloy systems with high glass forming ability along with the understanding of thermal stability of the amorphous matrix and evaluating the mechanical, magnetic, corrosion and other functional properties [202,206,343–348]. Owing to the presence of metalloids in BASs, the local clusters present in the liquid alloy are likely to be different from those in other BMGs. Structural relationships between the amorphous phases and those of crystalline phases formed after heat-treatment are going to be different in the two classes of BMGs. However, the volume of literature that explores the relationship between the structure of the nanocrystals with the local environment of the amorphous phase is very limited [343,349–353]. In addition, understanding the local structure, phase evolution and thermal stability in the framework of classical thermodynamics poses major challenge. Further, a few studies pertain to the stability of the amorphous matrix and the nature of the embedded nanocrystals in relation to the nature of synthesis processes [200,334,345,354–356]. Since, the melt spinning and thermal spraying are the variants of rapid solidification processes (RSP), their cooling rates vary between 10^5-10^7 K/s [212,330]. Change in cooling rates and heterogeneities in the alloys are known to affect the nucleation and growth behaviors. Local structure in the liquid alloy that is believed to be frozen in the amorphous state may marginally change it to facilitate the nucleation of nanocrystals depending on the experimental conditions. Detailed structural analysis of the amorphous phase and the nanocrystals that nucleate in the amorphous matrix may help in deciphering the structural correlation between the structural order in the glass and the nanocrystals. This understanding may hold the key to design nanocomposites with better combination of properties.

Present study deals with the synthesis of three Fe-based amorphous nanocomposite samples with nominal composition $Fe_{58.82}Cr_{11.12}Mo_{1.52}Si_{4.16}B_{15.12}P_{8.88}C_{0.39}$ (at.%) processed through three different routes, namely melt spinning, melt spinning followed by ball milling and thermal spraying (HVOF). Melt spinning and HVOF are likely to have very little deviation in the critical cooling rate. The microstructure is expected to evolve from a complex combination of critical cooling rate with the parameters associated with the process itself. The parameters that generally get changed with the methods of processing relate to sample thickness, nature of heat extraction etc. This work makes an attempt to understand the structural changes through XRD (X-ray Diffraction) and TEM (Transmission Electron Microscopy). Such an attempt will help establish the structural correlation of the nucleated nanocrystals with the amorphous ones. Semi-empirical thermodynamic model proposed by Miedema has been utilized to substantiate above findings.

6.2 Experiments

6.2.1 Synthesis

Alloy ingots of nominal composition $Fe_{58.82}Cr_{11.12}Mo_{1.52}Si_{4.16}B_{15.12}P_{8.88}C_{0.39}$ (at.%) were prepared by co-melting the ferro-alloys of Cr, Mo, Si, B and P along with mild steel scrap in a 4 kg air induction melting furnace. Once the whole charge is melted, melt is poured into pre-heated molds. The cast alloys produced after each heat are chemically analyzed by wet chemical analysis. After confirming the chemical composition, these alloys are further processed. The question of burning of P, B and C is taken care of by adding them in the charge in ferro form. In the ferro form the elements are trapped and their activity is reduced. This is how the elements are retained in the melt. In the as cast state segregation will always be there. However, the alloy is thermally sprayed and melt spun in order to kinetically bypass the otherwise equilibrium solidification route to avoid segregation.

Later, these alloy ingots were melt-spun to produce ribbons in a melt spinner (M/s Vacuum Technologies, Bangalore). Required quantity of the cast ingot is sliced and placed in a quartz crucible, which is fixed properly within the induction coil. The nozzle of the quartz tube is aligned such that the melt flows on to rotating Cu-wheel when ejected. The quenching wheel is water-cooled and is finely polished prior to melt spinning. The melt-spinning was performed in a vacuum chamber. This chamber was evacuated to 10^{-1} bar and flushed with high purity Ar-gas prior to melting. The speed of the Cu wheel was maintained at 2500 rpm during the experiment and an ejection pressure of 15 psi was used to eject the melt. Quartz crucible orifice diameter was 0.5 - 2.5 mm and the distance between the wheel and the crucible nozzle was 5 -10 mm. The width and thickness of the melt spun ribbons were measured to be ~20 mm and ~40 µm respectively.

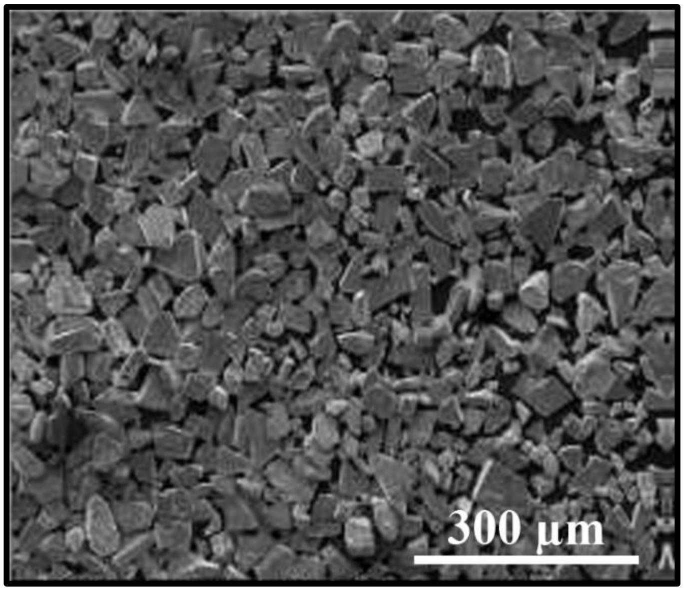

Figure 6.1: *FE-SEM image of the sieved powder after ball milling.*

Vibratory cup mill (Pulverisette 9, M/s Fritsch) was used to grind the ribbons to produce powder. Milling was done at a stretch of 2 min and was given a break for 2 min before next milling to avoid any heating of the ribbons. The cycle was repeated for 15 times. The shape and the size of the powder particles are mostly irregular after ball milling. Powder thus produced was sieved and the 38-65 µm size fraction was separated. The FE-SEM image of the milled and the sieved powder is given in the Figure 6.1. The flowability of the powder was measured in Hall flowmeter (Make: Alcan Metal Powder). The flowability of the milled and sieved powder turned out to be 50 g/s. Subsequently the powder was used as feed stock for thermal spraying. Coatings of the milled powder was deposited via High velocity Oxy-fuel (HVOF) spraying (model-HIPOJET-2700, MEC, India) onto cold rolled close annealed (CRCA) mild steel substrate. Composition of mild steel is given in Table 6.1.

Table 6. 1: *Mild steel composition details*

Elements	Si	C	P	Cr	V	S	Ni	Ti	Nb	Fe
Wt%	0.012	0.004	0.011	0.016	0.013	0.011	0.009	0.001	0.001	Rest

Single torch pass was given during the deposition of thermal spray (HVOF) coating. HVOF process parameters for the deposition of coatings were kept fixed and details are presented in table 6.2.

Table 6.2: *Process parameters for High Velocity Oxy Fuel (HVOF) spraying.*

Spray Parameters	**Coating sample**
Oxygen flow rate, (SLPM)	240
Fuel gas flow rate, (SLPM)	60-65
Air flow rate, (SLPM)	400
Powder feed rate, (g/min)	35
Spray distance (mm)	150
Torch passes (No.)	1

6.2.2 Characterization

Structural investigations of the amorphous phase and the nano-crystallites embedded in the amorphous matrix in the melt-spun ribbon, melt-spinning followed by ball milled powder and thermal spray (HVOF) coating samples were carried out by X-ray diffraction (MiniFlex600, RIGAKU) using Cu-K_α radiation. The operating conditions were kept at 40 kV of accelerating voltage and 15mA of current. In order to study the phase evolution, microstructure, state of ordering and interface structure of the powder, ribbon and coating samples, electron transparent specimens were prepared. A few milligrams of the high energy ball milled power was suspended in 5 mL ethanol and was ultrasonicated for about 10 min. From the top portion of the ultrasonicated suspension ~50 µL was sucked with the help of a micropipette and it was drop cast onto a carbon coated copper grid. The as cast grid was dried under infrared lamp for ~45 min before the grid was transferred to the microscope. As the sample was collected from the top portion of the suspension, it contained mostly the very fine floating particles. Thus, the electron transparency of the powder particles was ensured. For the ribbon and thermal spray (HVOF) coating samples, the electron transparent conventional and cross-section specimens were prepared by grinding, dimpling and ion beam thinning. Ion beam polishing was carried out with Gatan PIPS with Ar-ions operated under 5keV. Atomically resolved phase contrast imaging, diffraction contrast imaging and diffraction experiments were carried out in a Tecnai G^2 T20 (C_s= 1.2 mm) TEM operating at 200 kV.

6.2.3 Multislice simulation and diffraction patterns

High-resolution images and diffraction patterns were simulated for cI58 (FeCrMo), cF118 ($Fe_{18}Cr_6Mo_5$), oC68 ($Fe_{62}Cr_{34}Mo_4$), tP60 ($Fe_{64}Cr_5Mo_4$), tP58 ($Fe_{62}Cr_{34}Mo_4$), oP30 (Fe_2B_7), cI2 (α-Fe) and mI32 (Fe_5C_2) structures by JEMS [158]. The images along particular zone axes were simulated by multislice method keeping relevant parameters in conformity with those of experimental conditions. Diffraction patterns were computed under multiple beam dynamical condition. Crystallographic details of the phases, which have been used for simulation are given in the table 6.3 (a-c). Coding was done in MATLAB software in order to do the Miedema calculations.

6.3 Results

6.3.1 X-ray diffraction

Figure 6.2 represents the X-ray diffraction patterns of powder, ribbon and coating samples. The effects of each of the two RSP variants mentioned in the experimental section and ball milling post RSP can be noted in XRD patterns shown in figure 6.2. In the XRD pattern of the powder and in the thermal spray (HVOF) coating, a few broad and less intense peaks are observed. There is a diffused diffraction halo, which is mostly suppressed in the background due to the presence of the peaks. In contrast to this, the XRD pattern corresponding to the melt-spun ribbon sample appears to be amorphous. Such a behavior may be attributed to the higher cooling rate during melt spinning.

As mentioned above, XRD pattern of the powder displays a few broad peaks. In addition to this, moderately intense peaks can also be observed in the range of 2θ ~37.5°- 54°. Similarly, a few even less intense and broad peaks are observed in the range of 2θ ~ 72°- 85°. These peaks match with a number of carbide and intermetallic phases. The phases are marked with appropriate legends in figure 6.2. The details of the expected phases along with the respective d-spacings and corresponding hkl planes are given in the tables 6.3(a-c). It is important to point out that a diffuse diffraction hump is present in the same angular range, which is partly suppressed due to the presence of the crystalline peaks. It is inferred that the powder is not completely crystalline but has remnant amorphous phase. Moreover, the presence of the amorphous halo as a background to the crystalline peaks indicates that there might be a correlation in terms of near neighbor distance and coordination environment between the amorphous phase and the crystalline phases.

Table 6.3a: *Structural parameters used in multi-slice simulation cF118, oI92, and oC68 structures*

S.No.	**Struc.**	**Lattice Parameter (nm)**	**Space Group (No.)**	**Wyckoff Positions (Site)**	**Coordinates**			**Occ. (%)**
1	cF118	a=b=c= 8.92 Å	F$\bar{4}$3m (216)	Cr1 (48h)	0.356	0.356	0.042	0.375
		α=β=γ= 90^{0}		Fe1(48h)	0.356	0.356	0.042	0.625
				Cr2(48h)	0.089	0.089	0.278	0.125
				Fe2(48h)	0.089	0.089	0.278	0.875
				Mo1(4a)	0.000	0.000	0.000	1.000
				Mo2(16e)	0.317	0.317	0.317	1.000
2.	oI92	a= 9.79 Å	Imma (74)	Cr0 (16j)	0.398	0.398	0.000	0.333
		b= 8.79 Å		Fe1(16j)	0.398	0.398	0.000	0.333
		c= 3.55 Å		Mo2(16j)	0.398	0.398	0.000	0.333
		α=β=γ= 90^{0}		Cr3(16j)	0.739	0.066	0.000	0.333
				Fe4(16j)	0.739	0.066	0.000	0.333
				Mo5(16j)	0.739	0.066	0.000	0.333
				Fe6 (16j)	0.182	0.182	0.251	0.333
				Fe7(4a)	0.000	0.000	0.000	0.333
				Mo8(4a)	0.000	0.000	0.000	0.333
				Cr9(16j)	0.182	0.182	0.251	0.330
				Mo10(16j)	0.182	0.182	0.251	0.330
				Fe11(16j)	0.463	0.131	0.000	0.333
				Cr12(4a)	0.000	0.000	0.000	0.333
				Cr13(16j)	0.463	0.131	0.000	0.333
				Mo14(16j)	0.463	0.131	0.000	0.333
3.	oC68	a= 8.99 Å	Ccce (68)	Cr0 (16i)	0.398	0.398	0.000	0.333
		b= 8.79 Å		Fe1(16i)	0.398	0.398	0.000	0.333
		c= 4.35 Å		Mo2(16i)	0.398	0.398	0.000	0.333
		α=β=γ= 90^{0}		Cr3(16i)	0.739	0.066	0.000	0.333
				Fe4(16i)	0.739	0.066	0.000	0.333
				Mo5(16i)	0.739	0.066	0.000	0.333
				Fe6 (16i)	0.182	0.182	0.251	0.333
				Fe7(4a)	0.000	0.000	0.000	0.333
				Mo8(4a)	0.000	0.000	0.000	0.333
				Cr9(16i)	0.182	0.182	0.251	0.330
				Mo10(16i)	0.182	0.182	0.251	0.330
				Fe11(16i)	0.463	0.131	0.000	0.333
				Cr12(4a)	0.000	0.000	0.000	0.333
				Cr13(16i)	0.463	0.131	0.000	0.333
				Mo14(16i)	0.463	0.131	0.000	0.333

Table 6.3b: *Structural parameters used in multi-slice simulation tP60, tP58, and mI32 structures*

S. No.	Struc.	Lattice Parameter (nm)	Space Group (No.)	Wyckoff Positions (Site)	Coordinates			Occ. (%)
1.	tP60	a=b= 9.29 Å	P4/ncc	Cr0 (16g)	0.398	0.398	0.000	0.333
		c= 4.05 Å	(130)	Fe1(16g)	0.398	0.398	0.000	0.333
		α=β=γ= 90⁰		Mo2(16g)	0.398	0.398	0.000	0.333
				Cr3(16g)	0.739	0.066	0.000	0.333
				Fe4(16g)	0.739	0.066	0.000	0.333
				Mo5(16g)	0.739	0.066	0.000	0.333
				Fe6 (16g)	0.182	0.182	0.251	0.333
				Fe7(4b)	0.000	0.000	0.000	0.333
				Mo8(4b)	0.000	0.000	0.000	0.333
				Cr9(16g)	0.182	0.182	0.251	0.330
				Mo10(16g)	0.182	0.182	0.251	0.330
				Fe11(16g)	0.463	0.131	0.000	0.333
				Cr12(4g)	0.000	0.000	0.000	0.333
				Cr13(16g)	0.463	0.131	0.000	0.333
				Mo14(16g)	0.463	0.131	0.000	0.333
2.	tP58	a=b= 8.59 Å	P4/nbm	Cr0 (8i)	0.398	0.398	0.000	0.333
		c= 4.75 Å	(125)	Fe1(8i)	0.398	0.398	0.000	0.333
		α=β=γ= 90⁰		Mo2(8i)	0.398	0.398	0.000	0.333
				Cr3(16n)	0.739	0.066	0.000	0.333
				Fe4(16n)	0.739	0.066	0.000	0.333
				Mo5(16n)	0.739	0.066	0.000	0.333
				Fe6 (16n)	0.182	0.182	0.251	0.333
				Fe7(2a)	0.000	0.000	0.000	0.333
				Mo8(2a)	0.000	0.000	0.000	0.333
				Cr9(16n)	0.182	0.182	0.251	0.330
				Mo10(16n)	0.182	0.182	0.251	0.330
				Fe11(16n)	0.463	0.131	0.000	0.333
				Cr12(2a)	0.000	0.000	0.000	0.333
				Cr13(16n)	0.463	0.131	0.000	0.333
				Mo14(16n)	0.463	0.131	0.000	0.333
3.	mI32	a= 12.08 Å	I2/m (12)	Fe0(8j)	0.000	0.250	0.561	1.000
		b= 5.05 Å		Fe1(8j)	-0.097	0.326	0.078	1.000
		c= 4.07 Å		C2(8j)	-0.107	0.042	0.285	1.000
		α=β= 90⁰		Fe3(8j)	-0.215	0.091	0.581	1.000
		γ= 105⁰						

Table 6.3c: *Structural parameters used in multi-slice simulation for oP30, cI58, and cI2 structures.*

S. No.	Struc.	Lattice Parameter (nm)	Space Group (No.)	Wyckoff Positions (Site)	Coordinates			Occ. (%)
1.	oP30	a= 16.96 Å	Pbam (55)	Fe0(2a)	0.000	0.000	0.000	1.000
		b= 10.65 Å		Fe1(4g)	0.125	0.139	0.000	1.000
		c= 2.89 Å		B2(8i)	0.022	0.080	0.183	1.000
		α=β=γ= 90°		B3(8i)	0.152	0.986	0.817	1.000
				B4(8i)	0.062	0.125	0.722	1.000
2.	cI58	a=b=c= 8.92 Å	I$\bar{4}$3m (217)	Cr1 (24g)	0.356	0.356	0.042	0.375
		α=β=γ= 90°		Fe1(24g)	0.356	0.356	0.042	0.625
				Cr2(24g)	0.089	0.089	0.278	0.125
				Fe2(24g)	0.089	0.089	0.278	0.875
				Mo1(2a)	0.000	0.000	0.000	1.000
				Mo2(8c)	0.317	0.317	0.317	1.000
3.	cI2	a=b=c= 2.86 Å	Im$\bar{3}$m (229)	Fe1(2a)	0.000	0.000	0.000	1.000
		α=β=γ= 90°						

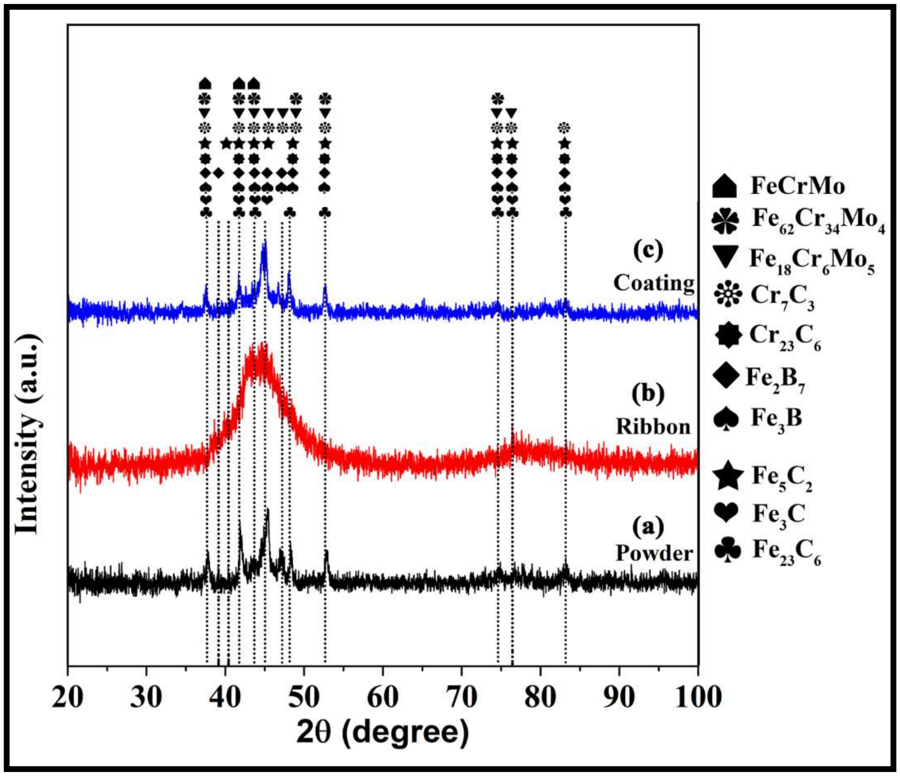

Figure 6.2: *Multiple display of X-ray diffraction patterns of the powder, ribbon and coating samples.*

The XRD pattern of ribbon appears to be amorphous having two broad humps lying in the range 2θ ~37.5°- 54° and 2θ ~72° - 85° respectively. Former is less diffuse than the latter. Changes in the nature of the diffuse humps can be attributed to the decrease in the form factor with the increase in the angle of diffraction. Additionally, they also represent different sets of near-neighbour distances and coordination environments. The first hump has its maximum intensity close to the d-spacing ~ 1.99 Å. This value is very close to the 110 plane of α- Fe. The second hump has its maximum intensity close to d-spacing ~ 1.2 Å. This d-spacing value is very close to 211 plane of α-Fe. The first and the second diffraction humps may be correlated with the existence of SRO and MRO in the amorphous phase respectively. However, its close similarity with the d-spacings of Fe may indicate the structural similarities of the SROs and MROs with Fe as it has been pointed out in earlier literature [357]. However, detailed insight about the coordination environment in the amorphous phase is not the main purpose of this study and will not be discussed further here.

In the XRD pattern of coating, a number of broad and less intense crystalline peaks are observed in the same 2θ range as observed in a diffraction pattern of the powder sample. The peaks cannot be indexed to any particular phase. However, they match with similar carbide and intermetallic phases, as was observed for the powder sample. In a similar line with the powder, in this diffraction pattern also, a diffused diffraction halo is observed, which is partially suppressed by the crystalline peaks. This naturally indicates that the coating is also not completely amorphous or crystalline. Rather it has got amorphous phase in the inter-crystalline region. It is worth pointing out that, the diffuse diffraction halo in all the three samples prepared through different processing routes appears over the same angular range. When they are considered in a standalone situation, all of them refer to similar near-neighbor distances and similar coordination environment. Unlike the case of melt-spun ribbon (Figure 6.2b), the two other samples (Figure 6.2a and 6.2c), the nucleation of crystalline phases could not be suppressed, consequent to this, sharp crystalline peaks are also observed along with diffuse humps. It is important to mention that the nature of remnant amorphous phase as well as those of crystalline ones in the powder and in the thermal spray (HVOF) coating appears to be similar. Crystalline phases arise owing to the glass forming ability of the nominal composition of the BAS. Major fraction of intermetallic phases observed as crystalline ones in this investigation fall in the class of Hägg phases.

Table 6. 4: *d-spacing values corresponding to their (hkl) planes for the observed phases*

d-spc. (nm)	**Expected Phases**									
	$Fe_{23}C_6$	**Fe_3C**	**Fe_5C_2**	**FeB**	**Fe_2B_7**	**$Cr_{23}C_6$**	**Cr_7C_3**	**$Fe_{18}Cr_6Mo_5$**	**$Fe_{62}Cr_{34}Mo_4$**	**FeCrMo**	**α-Fe**
0.643	(111)	-----	(200)	-----	(210)	(111)	-----	(110)	(110)	-----	-----
0.471	(200)	(100)	(110)	-----	(310)	(200)	-----	(200)	(200)	-----	-----
0.294	(222)	(101)	(310)	(110)	(001)	(222)	(040)	(310)	(211)	-----	-----
0.232	(331)	(110)	(020)	(101)	(321)	(331)	(150)	(321)	(022)	(002)	-----
0.212	(422)	(111)	(112)	(111)	(150)	(422)	(112)	(411)	(410)	(202)	(110)
0.193	(511)	(102)	(600)	(210)	(820)	(511)	(321)	(332)	(411)	(331)	-----
0.180	(440)	-----	(312)	(121)	(550)	(440)	(222)	(422)	(421)	(312)	-----
0.171	(531)	-----	(402)	(130)	(650)	(531)	(341)	(431)	(510)	-----	-----
0.160	(620)	(112)	(421)	(220)	(750)	(620)	(312)	(521)	(511)	-----	-----
0.152	(444)	(210)	(512)	(211)	-----	(444)	(332)	(530)	(530)	-----	-----
0.144	(640)	(211)	(422)	(131)	-----	(640)	(033)	(620)	(213)	(620)	(200)
0.130	(800)	(301)	(331)	(140)	-----	(800)	(143)	(631)	(630)	(631)	-----
0.122	(751)	(113)	(712)	(320)	-----	(751)	(333)	(721)	(720)	(721)	(211)

It is therefore believed that the coordination environment in the Hägg phases will bear some resemblance with that of the amorphous phase, which has been investigated in later section 6.4.1.

6.3.2 Mass-thickness and diffraction contrast imaging

In order to corroborate the XRD results from the powder, melt-spun ribbon and the thermal spray (HVOF) coating, the samples were observed under a transmission electron microscope (TEM) and they are given in figure 6.3(a-h). The bright field TEM (BFTEM) image of the powder and the corresponding diffraction pattern are given in figure 6.3(a-b). The size of the powder particles is in the range ~100-300 nm. The BFTEM image, shown in figure 6.3a, has been captured by selecting only the direct beam through selected area diffraction (SAD) aperture. This direct beam is collected within the 5° angle around the optic axis. Therefore, it is expected that this beam predominantly contains transmitted electrons and a few Bragg diffracted electrons, which are scattered at a very low angle. In the BF image randomly oriented, irregular shaped powder particles with mostly greyish regions with some distributed black regions could be observed. It is expected that the thicker regions are darker than the thinner regions. Additionally, the distributed black contrast may refer to some nanocrystals with little different chemistry than the amorphous matrix. Figure 6.3b represents the selected area diffraction pattern (SAD) obtained from the same region of powder sample. In the diffraction pattern a diffused halo is observed around the transmitted spot and within the halo a number of continuous or semi-continuous Debye rings and a few diffraction spots are embedded. The diffraction rings and the spots are having varying intensity. The presence of diffraction rings and the spots in the background of the diffraction halo confirms that the powder has got some crystalline phases embedded in the amorphous matrix.

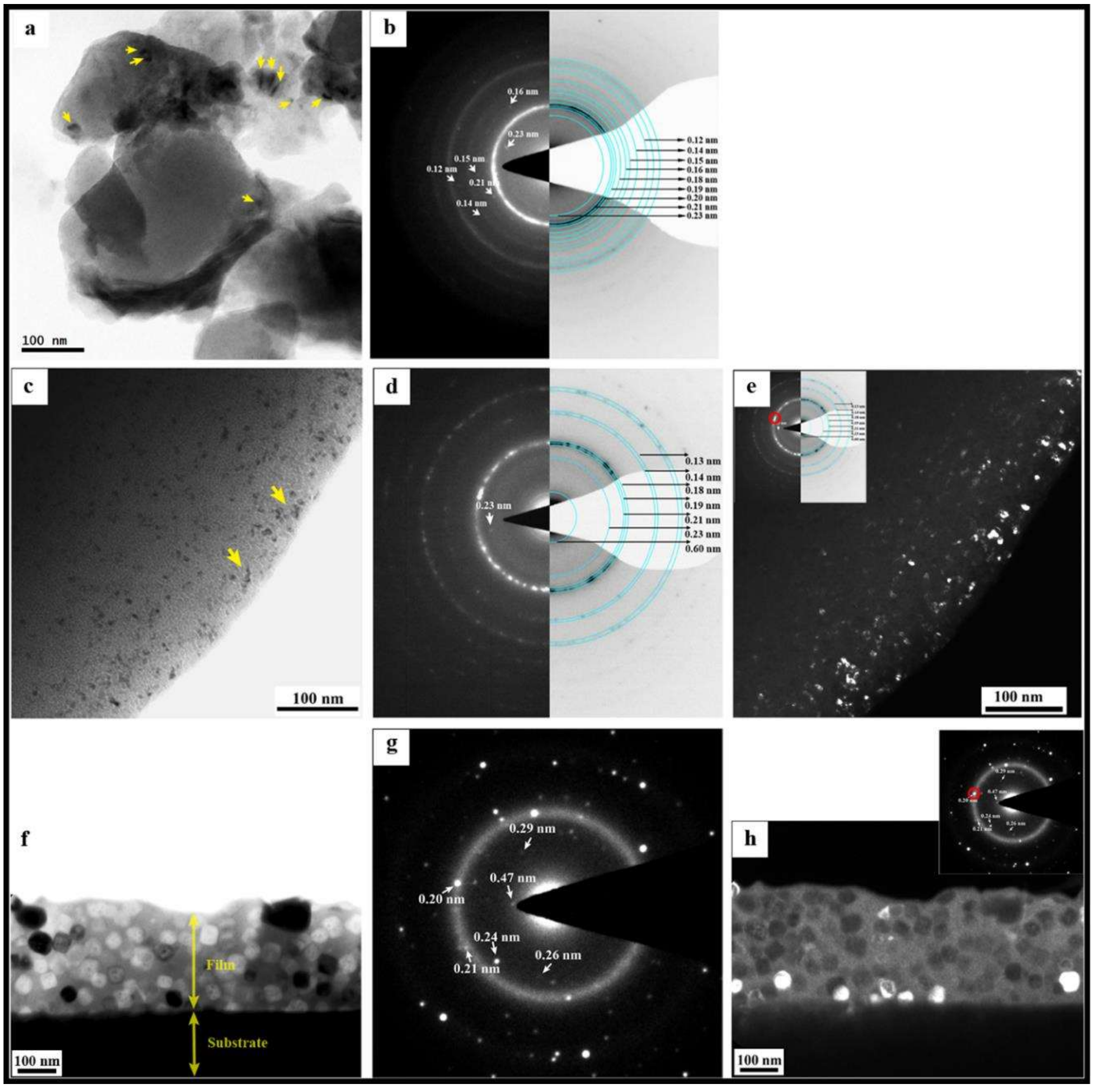

Figure 6.3: ***(a)*** *Bright field image of the powder,* ***(b)*** *corresponding diffraction pattern of the powder,* ***(c)*** *Bright field image of the ribbon,* ***(d)*** *corresponding diffraction pattern of the ribbon,* ***(e)*** *corresponding dark field image of the ribbon acquired by selecting a part of the ring encircled as shown in the inset,* ***(f)*** *cross-sectional bright field image of the HVOF coated sample,* ***(g)*** *corresponding diffraction pattern of the coated sample, and* ***(h)*** *corresponding dark field image of the coated sample acquired by selecting the spot encircled as shown in the inset.*

The same has been observed in the XRD pattern of the ball milled powder (Figure 6.2). In order to quantitatively analyze the diffraction rings, cyan colored semi-circular rings are superimposed onto the diffraction pattern. The d-spacings along with the expected phases as obtained from the analysis of the rings are given in the table 6.4. The d-spacings are in agreement with that of the XRD results. However, the d-spacings could not be unambiguously indexed to any particular phase. The bright field (BF) image, diffraction pattern and the dark field (DF) image from the melt-spun ribbon sample are given in figure 6.3(c-e). In the BF image (figure 6.3c) finely distributed nanocrystals in the size range of ~5-10 nm could be observed. The nanocrystals are predominantly faceted. The diffraction pattern in figure 6.3d corroborates with the BF image. A diffuse diffraction halo with a few spotty rings are observed (cf. Figure 6.3d). The spotty rings are overlaid with semi-circular cyan rings and the corresponding d-spacings are marked in the diffraction pattern itself. The d-spacings could not be indexed to any particular crystalline phase, rather they match with a number of similar type of phases as given in the tables 6.3 (a-c). In order to confirm the crystalline nature of the distributed black phase in the amorphous matrix, dark field (DF) image was recorded with a part of the diffraction ring as shown in figure 6.3e (inset) marked with a red circle. In the DF image, bright and uniformly distributed nanocrystals with irregular and faceted morphology could be observed. The nanocrystals are ~5-10 nm in size. This brings out an important difference with XRD pattern of the same sample. The pattern of the same sample is amorphous. However, the presence of crystalline phases in the amorphous matrix could be ascertained in the TEM investigation. It may be concluded that the volume fraction of the crystalline phase is not very high and the crystalline peaks appear in the same angular range as that of the diffuse halo. Hence, they could not be detected in the XRD. Further, this also indicates a structural relationship between the amorphous phase and the nanocrystalline phases in terms of their near neighbor environment.

Figure 6.3f represents the cross-section diffraction contrast image of the coating deposited onto the mild steel substrate. The substrate and the coating regions are marked separately in the figure. The contrast arising out of the substrate region is totally black, which may be attributed to its thickness. The interface between the coated film and the substrate is kept edge-on with respect to the electron beam while capturing the image. The interface region appears to be sharp at this magnification. The thickness of the coated film is found to be ~300 nm. Many faceted nanocrystals are present within the film region. The size of these nanocrystals is in the range ~ 5-50 nm. It appears that these faceted nanocrystals are oriented differently. The contrast associated with each of these individual crystals also varies. They appear as white, black and grey. This may be attributed to their difference in orientation. Additionally, local variation in chemistry may also play a role, which will be investigated later.

Figure 6.3g represents the SAD pattern obtained from the interface of the coating and the mild steel substrate. A few diffracted spots along with the diffuse halo may be observed in the diffraction pattern. This observation corroborates well with the image given in figure 6.3f. The substrate is crystalline and the film consists of a few nanocrystals embedded in the amorphous matrix. Figure 6.3h represents the dark field image acquired from the encircled spot shown in the inset. It is obvious that the diffracted spots are coming from the nanocrystalline features. Such dark field images have been recorded from many diffracted spots. However, none of them found diffracting from the grains of the substrate. This indicates that the substrate is quite thick and does not contribute to the SAD pattern. Intensity variation can also be seen in the diffracted spots as shown in figure 6.3g. This modulation in the intensity may be attributed to the different orientation of the nanocrystals, their deviation parameter value, structure factor, extinction distance etc. The higher intensity and randomness in the diffracted spots demonstrate that the nanocrystals are large in average size compared to the other two samples and they are oriented in various directions. The same is visible in figure 6.3f. The d-spacings corresponding to a few diffracted spots are marked in figure 6.3g. These d-spacings belong to certain number of phases whose details are given in the tables 6.4.

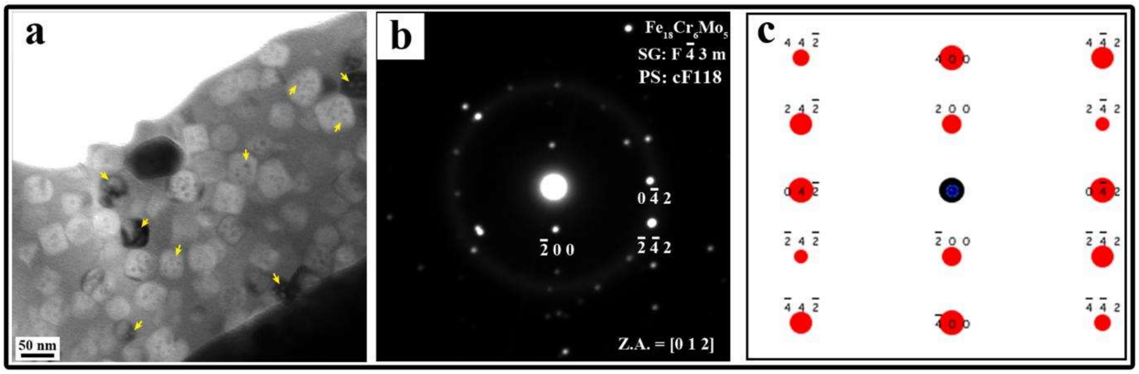

Figure 6.4: ***(a)*** *Bright field image of the cross-section of the coating,* ***(b)*** *corresponding diffraction pattern of the coating, and* ***(c)*** *simulated diffraction pattern of cF118 ($Fe_{18}Cr_6Mo_5$) structure along [012] zone axis.*

6.3.3 Identification of the faceted nanocrystals in the amorphous coating

The diffraction contrast in the BF image and the diffraction pattern of the cross section of the coating on the mild steel substrate are given in figure 6.4a and 6.4b. In the former, varying contrast of the nanocrystals could be easily discerned. As it has been stated earlier, the variation in contrast may primarily be attributed to the changes in orientation of the crystals. In addition to the orientation, their chemistry may also contribute to such a variation. Figure 6.4b shows SAD pattern acquired from the film region shown in figure 6.4a. While analyzing this diffraction pattern, it was found that many of the crystals are close to [012] zone axis of $Fe_{18}Cr_6Mo_5$ phase. However, when the diffraction pattern of the same phase along [012] zone axis with Pearson symbol cF118 and space group $F\bar{4}3m$ is simulated (Figure 6.4c), it shows up an excellent match with the experimental pattern. The structural parameters of this structure, which is used as an input file in simulation are given in table 6.3a. Although in the present case, the nanocrystals are embedded in amorphous matrix, still the match is quite good. Within the nanocrystals, finely distributed spotty contrast is observed (marked with yellow arrow in figure 6.4a). The reason behind this contrast is not quite clear. However, it might be attributed to the presence of amorphous phase around the crystals.

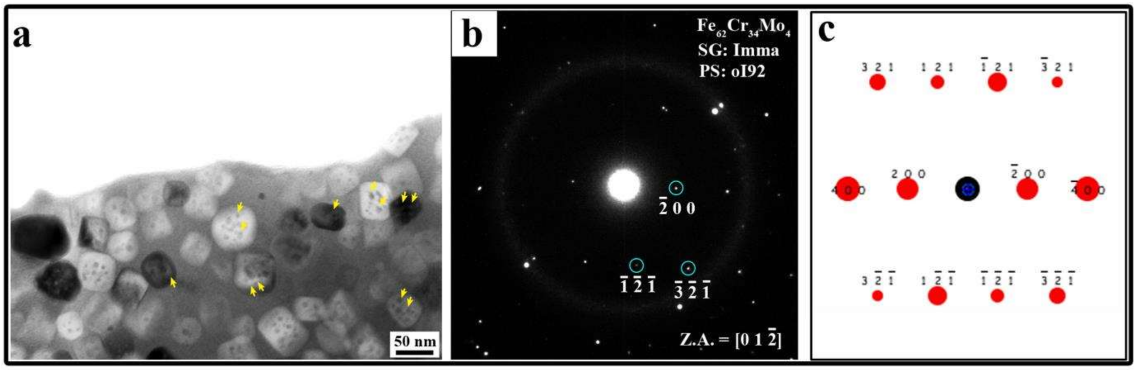

Figure 6.5: ***(a)*** *Bright field image of the cross-section of the coating,* ***(b)*** *corresponding diffraction pattern of the coating, and* ***(c)*** *simulated diffraction pattern of oI92 ($Fe_{62}Cr_{34}Mo_4$) structure along $[01\bar{2}]$ zone axis.*

Further, local variation in chemistry in the crystal or nucleation of some other related phase may be contributing to the observed contrast. In order to confirm the presence of any other phase along with the $Fe_{18}Cr_6Mo_5$ phase, various regions of the coating were observed from different electron beam directions. The bright field image and the corresponding diffraction pattern from some of the regions of the coating are given in figure 6.5(a-b). Faceted nanocrystals in the amorphous matrix could be clearly discerned (cf. Figure 6.5a). The size of the crystals varies in the range of ~5-50 nm. The diffraction pattern in figure 6.5b could be indexed based on $Fe_{62}Cr_{34}Mo_4$ phase, which is stoichiometrically different from the phase that was observed in the other region. When the diffraction pattern of the same phase along $[01\bar{2}]$ zone axis with Pearson symbol ‘oI92’ and space group ‘Imma’ is simulated (Figure 6.5c), it resembles with the experimental pattern. Although, we do not expect the exact intensity match as discussed earlier in this section. The details of the structure derived from this simulated pattern are given in a table 6.3a. It is confirmed from this experiment that Fe-Cr-Mo phase is predominant in the faceted nanocrystals with variation in stoichiometry and structure. There might be a polymorphic relationship between the structures, which will be explored and discussed in the subsequent sections.

6.3.4 Atomically resolved phase contrast imaging

Figure 6.6 represents the atomically resolved phase contrast image of a ball milled powder particle. In the image continuous fringe contrast is observed. However, at the top center of the image moiré pattern is observed and it is marked with arrows. Presence of moiré fringes indicates translational or rotational alignment of two structurally similar or nearly similar crystallites. On either side of the moiré pattern a continuous change in the contrast in the atomically resolved image is observed and they have been marked with differently colored windows (1-5). Local change in contrast in atomically resolved phase contrast image may be attributed to change in defocus and thickness, and change in structure and chemistry. In order to substantiate the change in contrast, the FFT (Fast Fourier Transform) from each of the regions marked with colored window has been obtained and they are presented in figure 6.7 (a-e). It can be seen from the FFTs in these figures that there are some structural changes taking place within the particle. The FFT in figure 6.7a has been obtained from the window ‘1’ in figure 6.6. The value of d-spacings as obtained by measuring the spots in the FFT as shown in figure 6.7a correspond to ~0.262 nm and ~0.209 nm respectively. The simulated pattern matched closely with the experimental FFT as shown in figure 6.7a. This structure is confirmed as an oC68 structure having space group Ccce. This appears to be a new observation. The details of this structure are given in the table 6.2. On analyzing this oC68 structure along $[\bar{2}3\bar{2}]$ zone, the spots are indexed as (221) and $(\bar{2}02)$ planes with d-spacing values ~0.262 Å and 0.209 Å respectively.

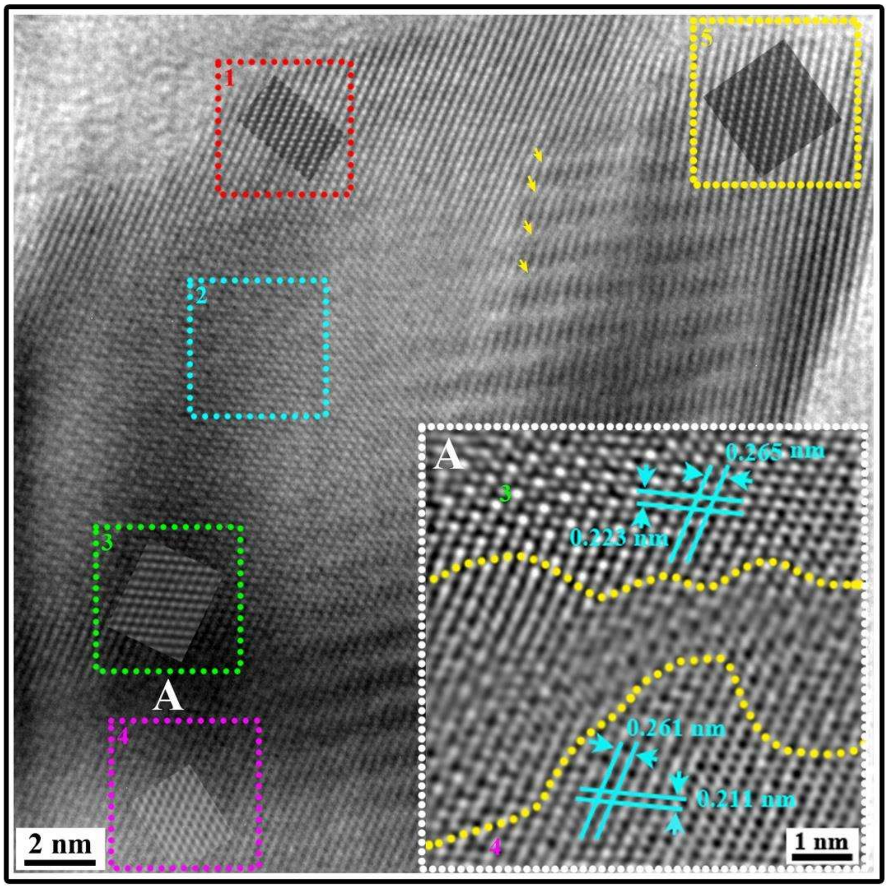

Figure 6.6: *Atomically resolved phase contrast image of the powder specimen. Each square box (1-5) represents variation in phase contrast. Inside the square boxes (1,3,4 and 5), superimposition of their corresponding multislice simulated images is shown. Inset 'A' represents the zoomed-in version of the region 'A'.*

The FFT acquired from the square window marked as '2' in figure 6.6 is given in figure 6.7b. It can be observed from the FFT that the extra spots are visible compared to the previous FFT acquired from the square window '1'. The phase contrast of the region as marked by window '1' is different from that of the square window '2' as evident in figure 6.6. This certainly indicates that a localized structural change is taking place from window '1' to window '2' in figure 6.6. The measured d-spacings of the chosen spots in the FFT (Figure 6.7b) are found to be ~ 0.401 Å and ~0.363 Å. The simulated pattern matched closely with the experimental FFT as shown in figure 6.7b. This structure is confirmed as a tP60 structure having space group P4/ncc. The details of this structure are given in the table 6.3b. On analyzing this tP60 structure along $[\bar{1}\bar{2}1]$ zone, the spots are indexed as (101) and $(\bar{1}11)$ planes with d-spacing values ~ 0.401 Å and ~ 0.363 Å respectively. This structural variant has not been reported in literature.

A definite change in phase contrast is observed in the square window '3' in figure 6.6. The FFT of the corresponding region is given in figure 6.7c. In this FFT the d-spacings values of the observed spots are approximately similar as obtained in the previous case for $Fe_{62}Cr_{34}Mo_4$ (tP60) structure (space group: P4/ncc, a= 0.929 nm and c= 0.405 nm). Also, the simulated diffraction pattern for this structure is exactly matching with the experimental FFT as shown in figure 6.7c. This confirms the presence of this structure within this region of the particles. In addition to this, a few extra spots at regular intervals are observed along 321 reciprocal vectors (encircled in yellow color). This might be due to the anisotropic ordering along this direction. This could also be a structural variant of the $Fe_{62}Cr_{34}Mo_4$ phase as reported in literature [330]. The appearance of the phase contrast image in square window '4' in figure 6.6 is quite different from those of other windows. The FFT from this window is given in figure 6.7d. The value of d-spacing measured for the spots encircled (red) is ~ 0.199 nm. This d-spacing value is different from what it was for the same spots in figure 6.7(a-c).

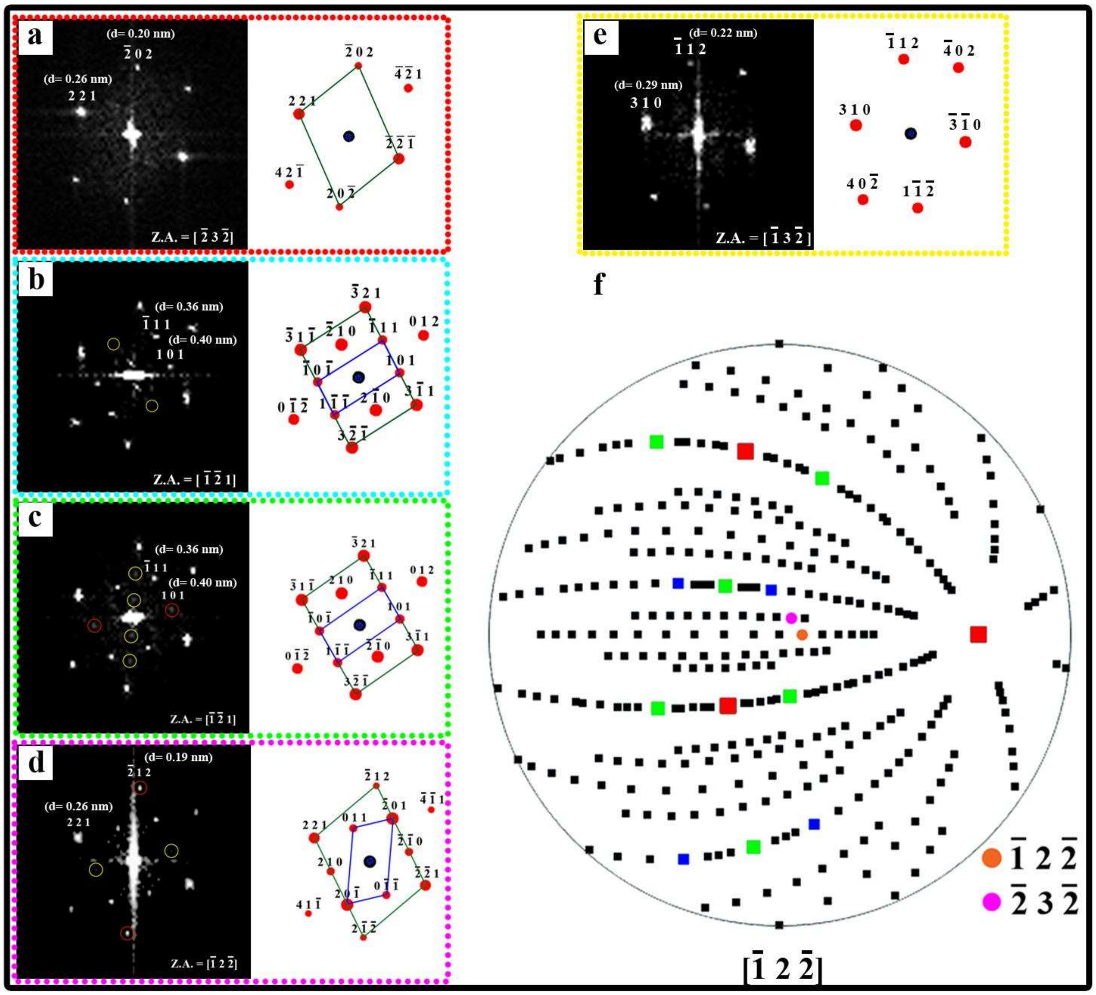

Figure 6.7: ***(a)*** *Experimental FFT and simulated diffraction pattern corresponding to square box '1' (figure 6.6) representing oC68 (Fe$_{62}$Cr$_{34}$Mo$_4$) structure along [$\bar{2}3\bar{2}$] zone axis,* ***(b-c)*** *experimental FFT and simulated diffraction pattern corresponding to square box '2 and 3' (figure 6.6) respectively, both represent tP60 (Fe$_{62}$Cr$_{34}$Mo$_4$) structure along [$\bar{1}\bar{2}1$] zone axis* ***(d)*** *experimental FFT and simulated diffraction pattern corresponding to square box '4' (figure 6.6) representing tP58 (Fe$_{62}$Cr$_{34}$Mo$_4$) structure along [$\bar{1}2\bar{2}$] zone axis,* ***(e)*** *experimental FFT and simulated diffraction pattern corresponding to square box '5' (figure 6.6) representing mI32 (Fe$_5$C$_2$) structure along [$\bar{1}3\bar{2}$] zone axis, and* ***(f)*** *Stereographic pole figure for the tP30 (Fe$_{62}$Cr$_{34}$Mo$_4$) structure along [$\bar{1}2\bar{2}$] zone axis showing that its structural polymorphs are also oriented along a nearby zone axis.*

This indicates that either this structure is different from the previous one or it is same but rotated to some nearby zone axis. On simulating the diffraction pattern for $Fe_{62}Cr_{34}Mo_4$ (tP58) structure along $[\bar{1}2\bar{2}]$ zone axis, a close match was found with the FFT as shown in figure 6.7d. The value of d-spacings of the spots corresponding to $(\bar{2}12)$ and (221) planes are ~0.264 nm and ~ 0.199 nm respectively. Now the structure is confirmed as a tP58 structure with the space group P4/nbm. The details of the structural parameters used for the simulated diffraction pattern is given in the table 6.3b. On careful analysis of the FFT shown in figure 6.7d, it has been observed that the spots encircled (yellow) are hardly visible. This might be attributed to the minor misalignment of the electron beam from the exact zone axis. It is quite clear from these observations that the ball milled powder particle while solidification and subsequent milling did not have enough time to attain equilibrium structure, rather different parts of the particle deformed/strained to a variable extent resulting in local structural variations leading to different non-equilibrium phases. In order to reduce its structural energy, polymorphism and local orientation adjustments are the key mechanisms of relaxation process. In order to understand such a process, the directional stereogram for tP30 ($Fe_{62}Cr_{34}Mo_4$) with $[\bar{1}2\bar{2}]$ as its central pole is given in figure 6.7f. It is obvious that the $[\bar{1}2\bar{2}]$ and $[\bar{2}3\bar{2}]$ poles are quite close to one another. Under the condition of non-equilibrium solidification and subsequent milling this much of localized orientational adjustment is possible to reduce the total structural energy.

In order to investigate the reason behind the black contrast and the invisibility of the fringes between the structures in square windows '3' and '4', the region marked as 'A' in figure 6.6 has been zoomed-in and shown as an inset. In this zoomed-in image, the region between two crystalline variants, as demarcated by yellow dotted lines, is quite strained, which has resulted in blurriness of the region. On careful observation, a significant amount of mismatch is found between the two crystalline domains. These polymorphs are present on either side of this strained region. It has been found that the mismatch between the fringes associated with d-spacing ~ 0.265 nm and ~0.261 nm of these structural polymorphs is ~1.5 % whereas the mismatch corresponding to d-spacings ~0.223 nm and ~0.211 nm is ~5.6%. Such a mismatch might have arisen due to structural adjustment during solidification and subsequent milling. It might be two separate nucleation events in the same particle, which upon coalescence had to re-adjust the interfacial strain or it might lead to a structural change during ball milling. It is confirmed from the figure 6.6 (and inset) that structures marked by window '3' and window '4' is oriented along $[\bar{1}\bar{2}1]$ and $[\bar{1}2\bar{2}]$ zones respectively. This might be a reason for this significant value of strain and invisibility of fringes in this region. Figure 6.7e represents the FFT of the region marked in square window '5'. The values of the d-spacings measured from the chosen spots are ~ 0.297 nm and ~ 0.223 nm. These d-spacing values matched closely with the (310) and $(\bar{1}12)$ planes of the Fe_5C_2 phase. The simulated pattern closely resembles with the experimental FFT shown in figure 6.7e. This structure conforms to mI32 structure with a space group I2/m (Table 6.3b). The orientation relationship between oC68 ($Fe_{62}Cr_{34}Mo_4$) (cf. Figure 6.7a) and tP60 ($Fe_{62}Cr_{34}Mo_4$) (cf. Figure 6.7b) structures can be obtained as: $[\bar{2}3\bar{2}]_{oC68} \parallel [\bar{1}\bar{2}1]_{tP60}$; $(\bar{2}02)_{oC68} \parallel (\bar{3}21)_{tP60}$. The orientation relationship between structures tP60 (cf. Figure 6.7c) and tP58 (cf. Figure 6.7d) are found to conform to : $[\bar{1}\bar{2}1]_{tP60} \parallel [\bar{1}2\bar{2}]_{tP58}$; $(\bar{3}21)_{tP60} \parallel (\bar{2}12)_{tP58}$. It is evident from figures 6.6 and 6.7 that in the ball milled powder particle the oC68 phase is present. However, localized structural variation in the particle is observed within the particle itself. The mechanism behind such structural variation would be discussed later (section 6.4.2). In addition to this, the surface structure of the particle is unique and it shows localized structural variation. The high-resolution phase contrast image of the surface of the melt-spun and ball milled powder particle near the oC68 ($Fe_{62}Cr_{34}Mo_4$) phase and mI32 (Fe_5C_2) phase are given in figure 6.8(a-b).

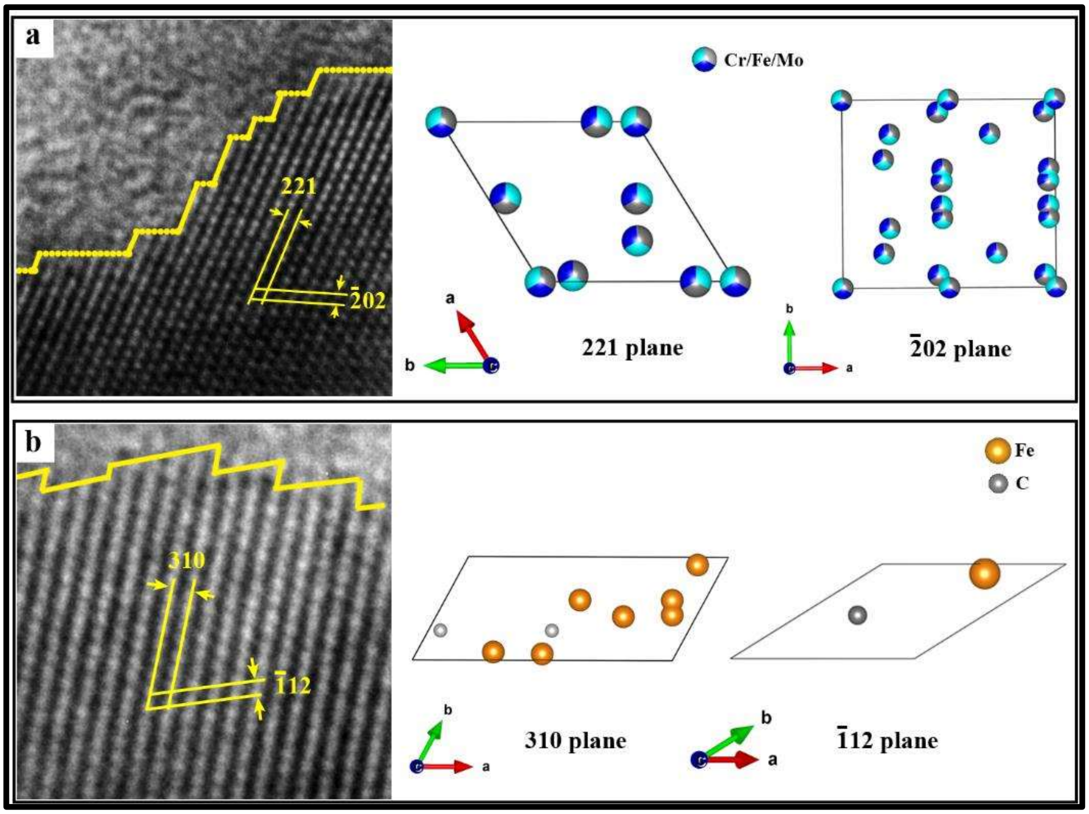

Figure 6.8: (a) *Atomic resolution phase contrast image of the oC68 ($Fe_{62}Cr_{34}Mo_4$) structure depicting facets at the interface. The (221) and ($\bar{2}02$) planes with respect to their relative atomic density are shown alongside, and* ***(b)*** *atomic resolution phase contrast image of the mI32 (Fe_5C_2) structure depicting facets at the interface. The (310) and ($\bar{1}12$) planes with respect to their relative atomic density are shown alongside.*

From the high-resolution image in figure 6.8a, it is obvious that the surface structure of oC68 ($Fe_{62}Cr_{34}Mo_4$) phase is kinked and ledged. The (221) plane and the ($\bar{2}02$) planes form the kinks and the ledges. The projection diagram of the (221) and ($\bar{2}02$) planes of the $Fe_{62}Cr_{34}Mo_4$ phase are given by the side of the high-resolution image. It appears that the atomic density of the (221) plane is less than that of ($\bar{2}02$) planes. Similarly, the high-resolution phase contrast image of the mI32 (Fe_5C_2) phase is shown in figure 6.8b. The surface structure near this phase also is kinked and ledged. The kinks and ledges are formed by (310) and ($\bar{1}12$) planes respectively. The projection diagram of the (310) and ($\bar{1}12$) planes are just beside the high-resolution image. The atomic density of the (310) plane is much higher than the atomic density of ($\bar{1}12$) planes. It can be briefly said that, even though the surface of the particle appears to be uniform, it has got kinks and ledges. The nature of the kinks and the ledges are also different depending on the local structure. Evolution of surface structure in the ball milled particle along with the variation in local structure will be discussed in section 6.4.

It has been observed that the ball milled powder particles are partially amorphous (cf. Figure 6.3a), in which nanocrystalline phases are embedded within the amorphous matrix. The crystalline phases also exhibit localized variation in the structure. The thermal spray (HVOF) coating of the same powder on mild steel substrate is also partially amorphous with some faceted nanocrystalline phases embedded in it. The crystalline phases are polymorphically transformed Fe-Cr-Mo intermetallics. The melt-spun ribbon sample also is partially amorphous with several H**ä**gg and other intermetallic phases. The nucleation of such phases, its local structure variation and its relation with the local structure of the amorphous alloy would require detailed understanding of the high-resolution phase contrast images. In order to understand the phase contrast images of oC68 (window'1' in figure 6.6), tP60 (window'3' in figure 6.6), tP58(window '4' in figure 6.6) and mI32 (window '5' figure 6.6) structures in a better way, multi-slice simulation has been done for each of these structures with respect to their atomic resolved phase contrast images. The simulated images of these structures have been superimposed onto the experimental one and shown in figure 6.6 under the square boxes.

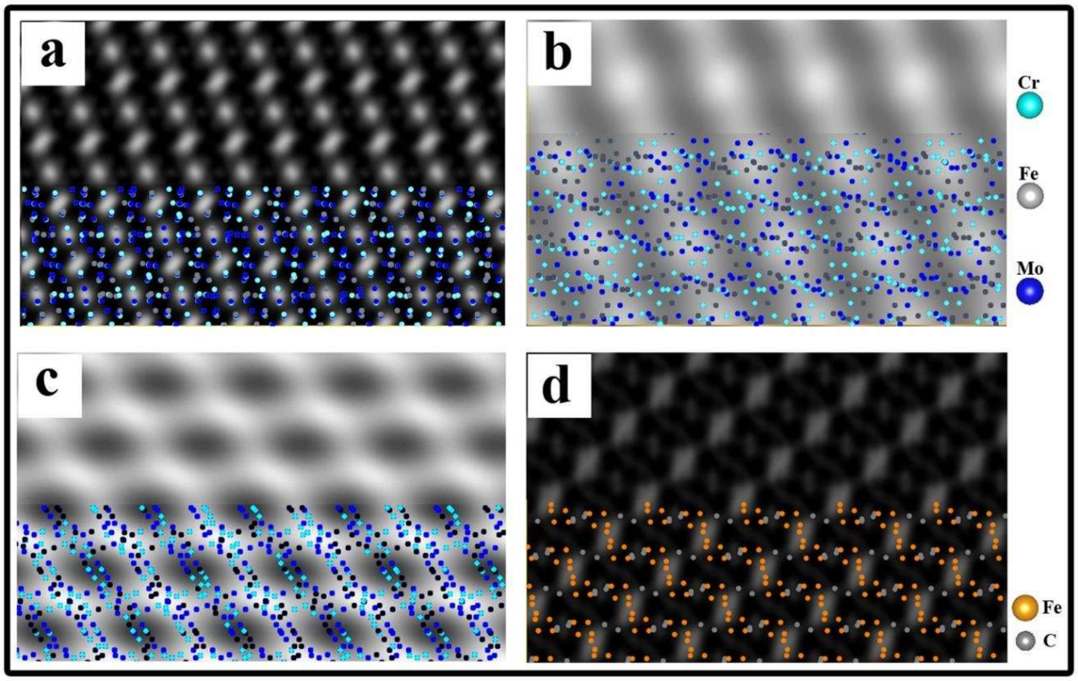

Figure 6.9: *Multislice simulated images along with the atoms overlay for* ***(a)*** *oC68 ($Fe_{62}Cr_{34}Mo_4$)* ***(b)*** *tP60 ($Fe_{62}Cr_{34}Mo_4$)* ***(c)*** *tP58 ($Fe_{62}Cr_{34}Mo_4$) and* ***(d)*** *mI32 (Fe_5C_2) structures respectively.*

It has been observed that these simulated images are in close match with the experimental one. The projected structures of these phases are overlaid onto their simulated images in figure 6.9(a-d). This is done in order to understand the contrast arising out of these structures clearly. Figure 6.9a represents the simulated image of the oC68 structure overlaid with the Fe, Cr, and Mo atoms along $[\bar{2}3\bar{2}]$ zone axis. In this image, it has been observed that mostly the black contrast is generated from the atomic clustered region whereas the white contrast is generated from the region where these atoms are arranged in a regular atomic column. Figure 6.9b represents the simulated image of tP60 (window ‘3’ in figure 6.6) structure along $[\bar{1}\bar{2}1]$ zone axis. The structure is quite complicated when projected along $[\bar{1}\bar{2}1]$ direction. The dark and bright contrast in the simulated image does not bear any direct correlation with the projected atomic columns of the structure. The simulated image of tP58 (window ‘4’ in figure 6.6) along $[\bar{1}2\bar{2}]$ zone is shown in figure 6.9c. The structural overlay on this simulated image is also shown in the same figure. It has been observed from this image that the alternate layers of the atomic clusters have not been imaged. The layers of atomic clusters that have been imaged have appeared white in contrast. The simulated image with the structural overlay of the mI32 (window’5’ figure 6.6) along $[\bar{1}3\bar{2}]$ is shown in figure 6.9d. One can clearly observe that the white contrast is coming from the Fe-atoms only. The carbon atoms are not being imaged but are located in the black contrast regions as shown in figure 6.9d. The atomically resolved high resolution image obtained from another particle in the ball milled powder sample is given in figure 6.10a. Two regions have been marked as ‘A’ and ‘B’ within this particle. The phase contrast appeared to be different within these regions.

The appearance of atomic fringes in region ‘A’ is quite regular compared to region ‘B’. A lot of distortion can be seen in the fringes of region ‘B’. Interface has also been marked within the square box so as to distinguish region ‘A’ from region ‘B’. In order to identify the structure in region ‘A’, FFT has been obtained from the same region and is shown alongside. After careful analysis, this FFT matches closely with the cI58 ($Fe_{18}Cr_6Mo_5$) phase. The same has been substantiated with the simulated diffraction pattern along $[0\bar{1}2]$ zone. Multislice simulation has been done for the region ‘A’ to appreciate phase contrast properly. The cropped experimental and simulated images are shown alongside for comparison. The experimental cropped region ‘A’ and its corresponding simulated image resembled well. The overlaid real structure of cI58 ($Fe_{18}Cr_6Mo_5$) along $[0\bar{1}2]$ zone axis shows that the cluster of Mo atoms are generating white contrast. The black and grey contrasts are arising from the atomically mixed cluster of Cr and Fe atoms. Moreover, moving from the region ‘A’ towards the region ‘B’, a lot of distortion has been introduced.

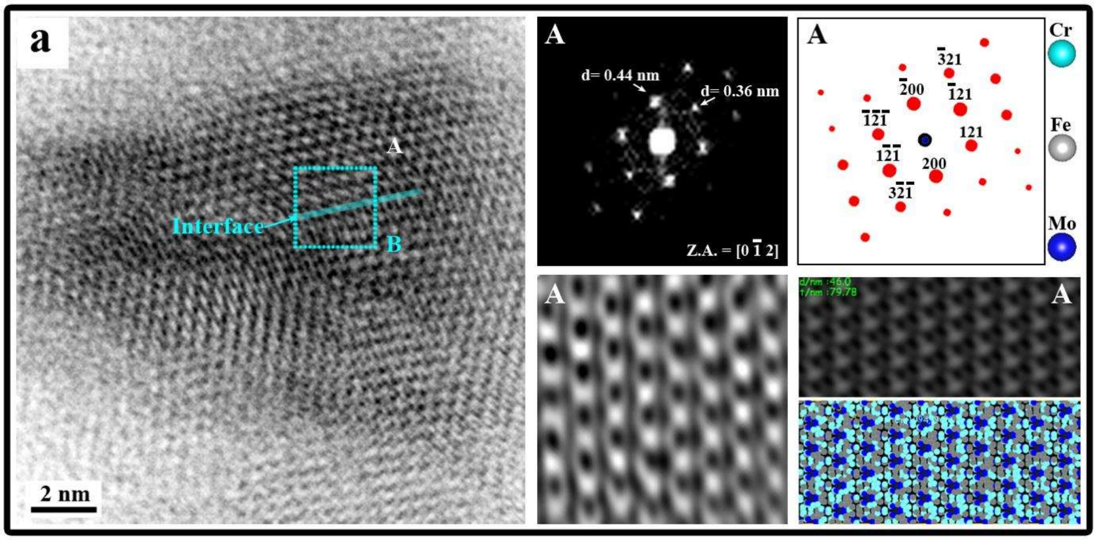

Figure 6.10: *High resolution phase contrast image of the powder specimen. Mark ‘A’ and ‘B’ represent undistorted and distorted regions across the interface. FFT obtained from region ‘A’ is shown along with the simulated diffraction pattern of cI58 structure. The cropped image of region ‘A’ (placed below FFT) is shown along with the multislice simulated image of cI58 structure with atoms overlay.*

Therefore, in order to understand this structural distortion taking place across the interface of the region ‘A’ and region ‘B’, the square region (cyan color) marked with dotted line is investigated in detail. The zoomed-in version of the same region has been cropped and shown separately in figure 6.11a. In this figure, five-line profiles (marked as ‘1-5’) have been drawn in order to show the structural changes happening across the interface. The variation in the relative columnar potentials and its separation distance within each line has been shown alongside (marked as “1-5”) in the figure 6.11a. It is worth-mentioning that the bright contrast refers to the Mo atomic clusters and the grey and dark contrast represents Fe and Cr atomic clusters respectively. It can be seen in the figure corresponding to line profile ‘1’ that the separation between the two consecutive Mo atomic cluster entities is ~ 0.46 nm. This spacing has increased to ~0.48 nm on moving near to the interface as

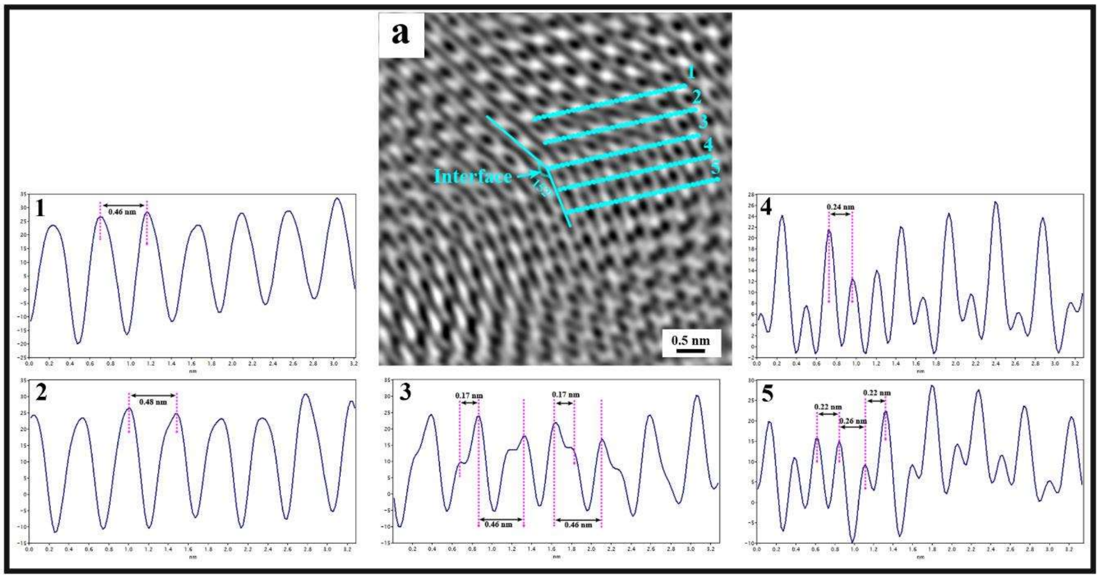

Figure 6.11: ***(a)*** *Zoomed-in image of dotted square box (cyan color) in figure 6.10. Line profiles (1- 5) represent lines (1-5) respectively in (a).*

represented in figure for line profile ‘2’. This is the evidence of strain present near the interface. At the interface as represented in figure for line profile ‘3’, a doublet can be seen with significant difference in the relative potentials. The spacing between the doublets is ~ 0.17 nm. The measured spacing between the two consecutive higher potential curves is ~ 0.46 nm. This indicates that the Mo clusters are broken at the interface. This rupture in the Mo clusters takes place at the interface which was ~0.46 nm apart away from the interface. Figure corresponding to line profile ‘4’ shows that the spacing between two consecutive atomic potentials has been reduced to ~ 0.24 nm. This value of spacing is approximately half the value measured in the previous line profile ‘2’. This indicates that the structural rearrangement has taken place. On moving further from the interface, the figure corresponding to line profile ‘5’ depicts that the spacing is further reduced to ~0.22 nm with some fluctuations in the values (~0.26 nm) towards right. This indicates that structural distortion takes place in the boundary, the nature of the interface is diffuse and the distortion is quite a few atom layers thick. Additionally, a rotation of ~ 152° across the interface is seen (Figure 6.11a).

High resolution phase contrast image of the melt-spun ribbon sample is shown in figure 6.12. This high resolution (HRTEM) image depicts the presence of nanocrystalline domains in an amorphous matrix. The size of these nanocrystalline domains lies in the range ~ 5-30 nm. In order to investigate the structures of these nanocrystalline particles, two different particles have been chosen at a significant distance, which are represented by the square boxes. These two square boxes have been designated by numerals ‘1’ and ‘2’ respectively.

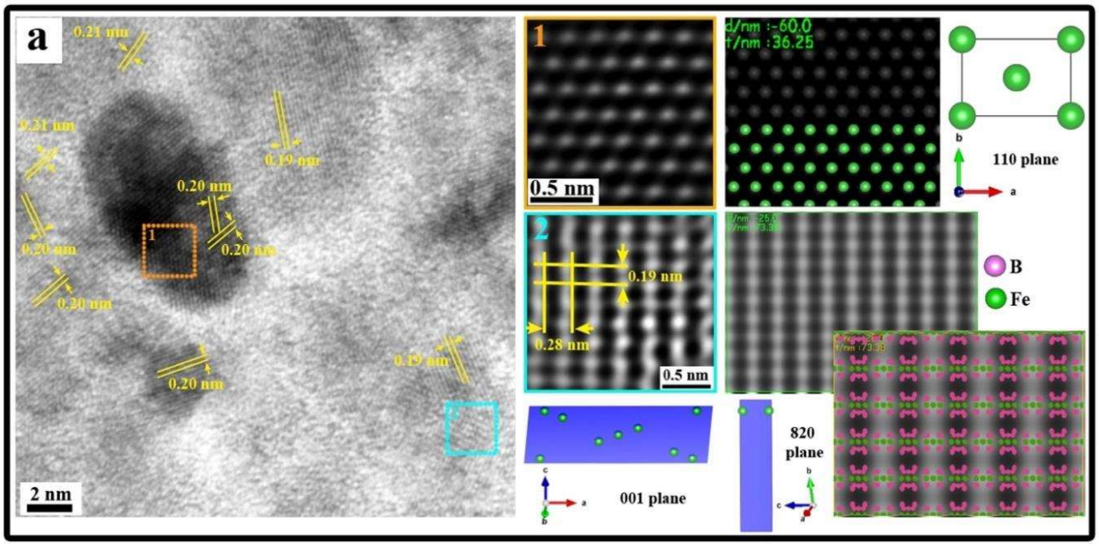

Figure 6.12: (a) *High resolution phase contrast image of the ribbon specimen. Outset 1 represents the magnified version of the cropped region 1 in (a). Multislice simulated image of cI2 (α-Fe) structure is shown alongside outset 1 with overlay of Fe atoms. The (110) plane of the same structure represents the surface with un-bonded Fe atoms. Outset 2 represents the magnified version of the cropped region 2 in (a). Multislice simulated image of oP30 (Fe_2B_7) structure is shown alongside outset 2 with overlay of Fe and B atoms. The relative atomic density associated with the (001) and (820) surface planes of the same structure has also been shown alongside.*

The region cropped from the nanocrystal marked under square box ‘1’ is shown separately as outset ‘1’. The closely matched multislice simulated image of this region has been shown alongside. This multislice simulation confirms that this structure belongs to α-Fe type and oriented along [111] zone axis. The value of d-spacing is ~ 0.202 nm and matches closely with the 110 planes of α-Fe. In order to understand the phase contrast of the experimentally obtained high resolution phase contrast image of α-Fe type structure shown as inset ‘1’, the real structure of α-Fe type viewed along [111] zone has been overlaid on the simulated image.

The superimposition of the real structure reveals that the white columnar contrast is coming from the Fe atoms only. This columnar contrast represents the 110 planes of the α-Fe type structure. The outset ‘2’ in figure 6.12 represents the zoomed-in version of high resolution image taken from the area marked under square box ‘2’. This experimental image has been analyzed further. The value of the d-spacings measured from this image are matching with the (001) and (820) planes of the Fe_2B_7 phase. This structure is orthorhombic with a space group ‘Pbam’ and Pearson symbol ‘oP30’. The lattice parameters are a=1.696 nm, b= 1.065 nm and c= 0.289 nm. The value of d-spacings corresponding to (001) and (820) plane are ~ 0.289 nm and ~0.197 nm respectively. The multislice simulated image for the same region is shown alongside. This simulated image of Fe_2B_7 structure closely matched with experimental zoomed-in image (outset 2).

The projected structure along [$\bar{1}$40] when superimposed on the simulated image, it is observed that the bright contrast is generated from a cluster of Fe and B atoms. However, the dark contrast is mostly explained by the presence of B atoms and the inter-columnar spaces. A careful analysis indicates that almost all the Fe atoms are imaged as bright contrast and only few B atoms around the Fe atoms are imaged. The number of un-bonded surface Fe atoms associated with the section of (001) and (820) planes are shown in the same figure (just below inset 2). This observation states that only Fe atoms are lying in these planes. Additionally, the atomic density of (001) plane is more than the (820) plane. Therefore, the surface energy associated with each of these planes may vary and play an important role in the growth process.

6.4 Discussion

6.4.1 Phase evolution, local structure and polyhedral order

As mentioned in the preceding sections, a Fe-based amorphous alloy forming system has been processed through three different processing routes, namely melt-spinning, melt-spinning followed by high energy ball milling and coating onto a mild steel substrate by thermal spraying (HVOF) starting with the ball milled powder. Even though the melt-

Table 6. 5: *Details of the phases obtained in the powder, ribbon and coating samples*

S.No.	Sample	Processing Route	Phases Obtained	Pearson Symbol	Space Group (No.)
1.	Powder	Ball Milling	$Fe_{18}Cr_6Mo_5$	cI58	$I\bar{4}3m$ (217)
			$Fe_{62}Cr_{34}Mo_4$	oC68	Ccce (68)
			$Fe_{62}Cr_{34}Mo_4$	tP60	P4/ncc (130)
			$Fe_{62}Cr_{34}Mo_4$	tP58	P4/nbm (125)
			Fe_5C_2	mI32	I2/m (12)
2.	Ribbon	Melt Spinning	α-Fe	cI2	$Im\bar{3}m$ (229)
			Fe_2B_7	oP30	Pbam (55)
3.	Coating	HVOF	$Fe_{18}Cr_6Mo_5$	cF118	$F\bar{4}3m$ (216)
			$Fe_{62}Cr_{34}Mo_4$	oI92	Imma (74)

spun ribbon is X-ray amorphous, finely distributed nanocrystals are observed in the amorphous matrix under transmission electron microscope. In the melt-spun ribbon, the nanocrystals are mostly cI2 (α-Fe) and oP30 (Fe_2B_7) phase. The same melt-spun ribbon after high energy ball milling results into nanocrystalline powder, in which nanocrystals of cI58 ($Fe_{18}Cr_6Mo_5$), oC68 ($Fe_{62}Cr_{34}Mo_4$), tP60 ($Fe_{64}Cr_5Mo_4$), tP58 ($Fe_{62}Cr_{34}Mo_4$) and mI32 (Fe_5C_2) phases are observed.

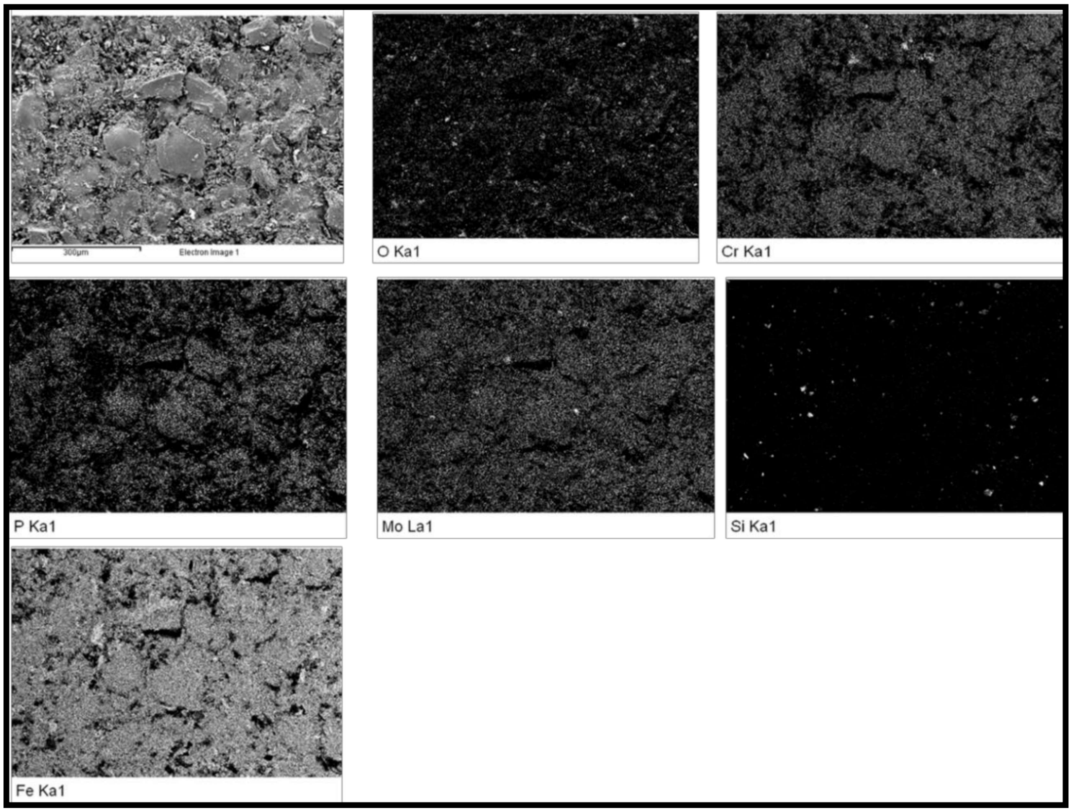

Figure 6.13: *Above image shows the surface compositional map through SEM-EDS of single layer coated samples. Uniform distribution of the major alloying elements like 'Cr', 'Mo', 'P' and 'Si' was observed in the coating. Distribution map of 'O' shows uniform oxidation at the coated surface.*

It is important to emphasize here that after ball milling the α-Fe and the Fe_2B_7 phases, which were present in the melt spun ribbon are not necessarily completely dissolved. However, the above mentioned intermetallic phases are observed. In the coating also cF118 ($Fe_{18}Cr_6Mo_5$) and oI92 ($Fe_{62}Cr_{34}Mo_4$) phases are observed. The phase evolution in this alloy system after processing through different routes has been summarized in table 6.5. Oxygen pick up is quite likely in the HVOF process, which has been adopted for the deposition of the coating. The oxygen pick up was investigated and it was found that such a pick up took place at the surface region of the film and in the inter-splat region.

FE-SEM based composition map of such oxygenated regions are given in the figure 6.13 and 6.14. As the oxygen pick up was mostly concentrated near the surface of the film, the signature of oxygen could not be found in the TEM study as during cross section sample preparation the near surface region is mostly lost during ion beam thinning.

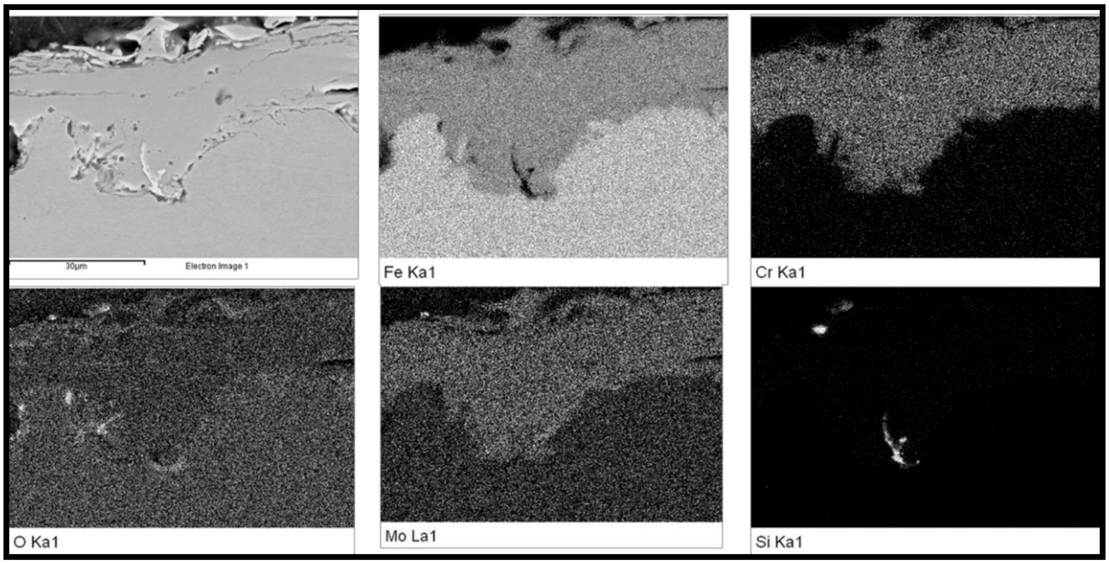

Figure 6.14: *Above image shows the elemental map of the coating cross-section obtained by using SEM-EDS across the single layer of coating. Here also uniform distribution of the important alloying elements was observed throughout the coating layer. The elemental map for 'O' in the image further substantiates the fact that limited oxidation was observed along the inter-splat boundaries.*

Fe-B, Fe-C and Fe-Cr-Mo intermetallic phases have been observed in Fe-based amorphous alloys upon crystallization. These are reported in earlier studies [330,358,359]. The Fe-B and Fe-C phases can broadly be classified as Hägg phases [360]. As the alloy composition in the present study belongs to a metal-metalloid system, it is quite natural to obtain Hägg phases as crystalline product in the amorphous matrix. Precipitation of such phases is one of the distinguishing factors of this glass forming alloy system with that of metal-metal glass forming alloy system. However, there are quite a few similarities also with them. In metal-metal glass forming alloy system also intermetallic phases with quite complex structures have been reported to precipitate during processing and crystallization. It has been reported in earlier literature that the structures of the intermetallic phases are related to the underlying structure of the glass as well as the liquid which is rapidly frozen to form the glass [202,342–344,349,350]. Detailed investigation on the structure of such phases has led to the conclusion that polyhedral structure exists in metal-metal glasses, which mainly belongs to Frank-Kasper polyhedra and Bernal deltahedra [361,362]. Often the polyhedra are distorted due to the presence of differently sized atoms in the glass forming compositions. However, such investigation in metal-metalloid glasses is limited [343].

It is important to point out here that such studies are important to establish any polyhedral order that might exist in the amorphous and in the liquid phases. The Fe-Cr-Mo intermetallic phases are crystallographically very different despite their stoichiometry being nearly the same. All the Fe-Cr-Mo phases obtained in the present study can be derived from the cI58 structure by suitably adjusting the lattice parameter and space group. The cI58 structure has been reported earlier and its crystallographic data are available in literature [205,330]. The crystallographic data for the derived phases has been given in the table 6.3(a-c). Coordination environment and underlying polyhedral structure for different

Fe-Cr-Mo intermetallic phases obtained in the present study are given in figure 6.15. It is observed that in cF118 ($Fe_{18}Cr_6Mo_5$) phase (Figure 6.15a), polyhedral structures are made out of a complex combination of distorted tetrahedra and octahedra. Similar types of coordination polyhedra comprising a complex combination of tetrahedra, pyramids, octahedra and truncated octahedra are found in oI92, oC68, tP60 and tP58 phases as shown in figure 6.15(b-e). In mI32 (Fe_5C_2) phase also tetrahedra, octahedra, their distorted combination, truncated version and distorted quadrilateral bipyramids are observed (Figure 6.15f).

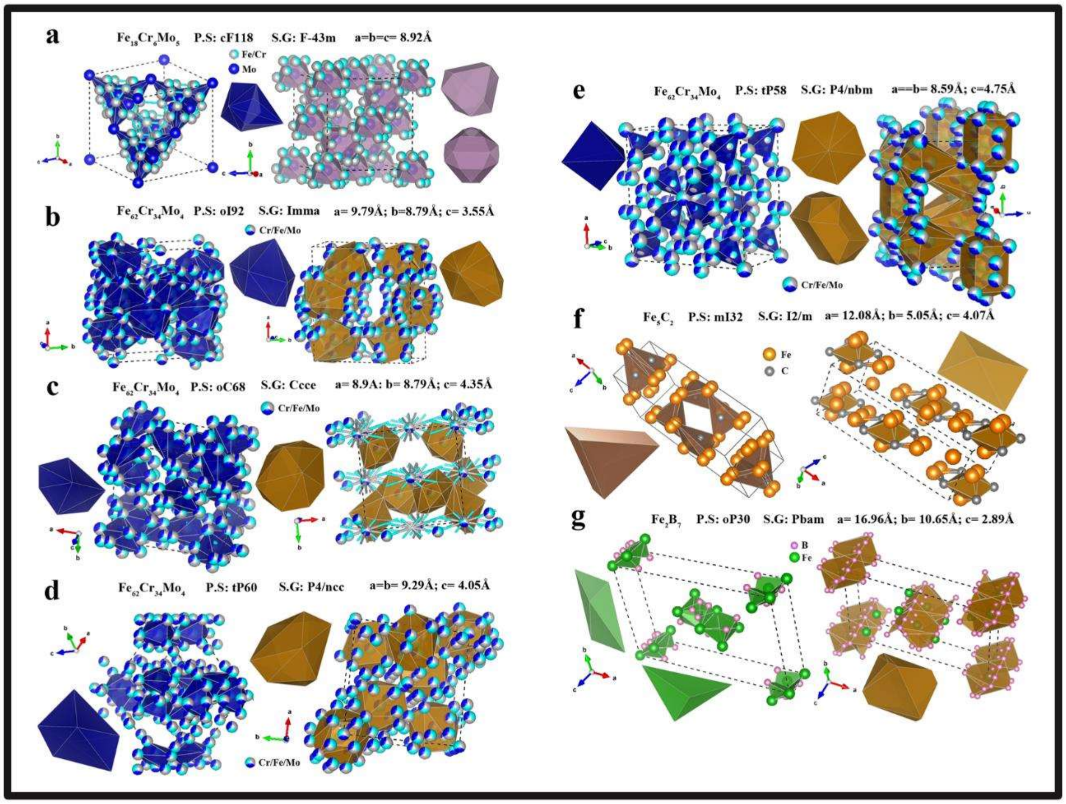

Figure 6.15: *Representation of polyhedrons associated with* ***(a)*** *cF118 ($Fe_{18}Cr_6Mo_5$),* ***(b)*** *oI92 ($Fe_{62}Cr_{34}Mo_4$),* ***(c)*** *oC68 ($Fe_{62}Cr_{34}Mo_4$),* ***(d)*** *tP60 ($Fe_{62}Cr_{34}Mo_4$),* ***(e)*** *tP58 ($Fe_{62}Cr_{34}Mo_4$),* ***(f)*** *mI32 (Fe_5C_2), and* ***(g)*** *oP30 (Fe_2B_7) structures respectively.*

In oP30 (Fe_2B_7) phase, similar polyhedral combinations are present (Figure 6.15g). The similarity of this metal-metalloid nanocomposite alloy with that of metal-metal nanocomposite alloy is that both gives rise to complex intermetallic phases upon crystallization [354,363]. In this alloy system, precipitation of H**ä**gg phase is seen, which is not possible in metal-metal amorphous alloys as metalloids are not present in those alloys. The phases precipitated in metal-metal amorphous alloys and nanocomposites are also having a polyhedral structure, which are mostly correlated to Frank-Kasper polyhedral and Bernal deltahedra [333,340–342]. However, in this nanocomposite, even though polyhedral structure is present in the precipitated phases, they cannot be directly correlated to Frank-Kasper polyhedra or Bernal deltahedra. This conclusion can further be extended as hypothesis that coordination polyhedra present in metal-metalloid amorphous alloys and nanocomposites are structurally different from those in metal-metal amorphous alloys and nanocomposites. It is likely that the coordination polyhedra in these two classes of liquids are also different.

6.4.2 Statistical nature of precipitation, phase selection and chemistry

The Fe-based amorphous phase forming alloy system has been processed through three different routes. In the melt-spun ribbon, which solidified at a cooling rate of 10^5-10^7 K/s, considerable amount of amorphous phase in which dispersed nanocrystals of α-Fe type and Fe_2B_7 phases are seen. Nucleation of such phases may be attributed to the random nucleation and succeeding growth either homogeneously or heterogeneously. High energy ball milling of the ribbon results into the nucleation of more nanocrystals in the amorphous matrix. The phases are mostly Fe-Cr-Mo intermetallic phase and Fe-C H**ä**gg phase. However, it does not ascertain that α-Fe type and Fe_2B_7 phases disappear after ball milling. Nucleation of such phases is mostly driven by the need to accommodate the strain energy that is imparted to the alloy during high energy ball milling and the rise in local temperature during the milling process [336]. The Fe-Cr-Mo intermetallic phases show local structural variation as has been established by electron microscopy and simulation. It can be inferred from this observation that all the structural variants of the Fe-Cr-Mo phase are also energetically very similar. It has been postulated before that the energy landscape for amorphous phase forming alloys is quite shallow and there are several local minima [205,345]. So many structural variants of Fe-Cr-Mo phase must be energetically very similar in order to undergo such changes very locally. Their structural correlation has been established in the earlier section [47]. It is also possible that all the structurally variant and energetically similar phases nucleated independently during ball milling and later they adjusted their orientation in such a manner that the interface energy is minimized. The probability of such event is quite limited as it will require orientational adjustment of the independently grown nuclei in solid state which by itself an energy intensive process. Additionally, the polymorphic transformations (oC68 → tP60 → tP58) have happened in such a way that hardly any interface amongst this structural transition is recognized. In the thermal spray (HVOF) coating also similar Fe-Cr-Mo intermetallic phase is obtained. However, the intermetallic phases are separated from one another and they are faceted. This further reinforces the point that interface energy between the crystals or the crystals and the amorphous matrix is important in determining its shape evolution [200,336,338,354,364–366]. It is worth-noting that there is an important difference between the Fe-B or Fe-C Hägg and the Fe-Cr-Mo intermetallic phases. In the former relatively larger atomic size difference may allow for substitutional and interstitial ordering depending on the energetics. In contrast, the Fe-Cr-Mo intermetallic phases will not display interstitial ordering owing to high value of the strain energy. It should also be borne in mind that in

HVOF process the shape and the size of the powder particles seriously affect the fluidity of the powder and in turn the phase and the microstructure evolution. The present work mostly deals with the relative comparison of the phase and the microstructure evolution after processing through different routes.

In the melt-spun ribbon, nanocrystals of ~5-20 nm size are dispersed in the amorphous matrix. Crystallization during subsequent ball milling was mostly driven by the energy imparted by the milling process. In thermal spraying (HVOF) also relatively more time was available for the alloy to solidify. So, the nucleated crystals could grow up from ~5 to 50 nm by optimizing their interface energy with the matrix. It is important to note here that change of substrate and its size may offer additional avenues of controlling microstructures of the crystalline phases in the amorphous matrix [342,367–369]. This opens up the possibility to tailor properties like wear, corrosion etc., in such kind of materials and coatings.

6.4.3 Complexities at the surfaces and interfaces

It has been observed in the present study that a number of phases are formed in the alloy after processing through different routes. Most of the phases are Fe-rich phases. However, it is difficult to identify them uniquely as their d-spacings are quite similar. For Fe-B and Fe-C based Hägg phases, different compounds have been reported with very similar d-spacings [359,370]. For Fe-Cr-Mo intermetallic phases, the lattice parameters are quite similar and it has been shown in this investigation that they can be derived from each other. It has been done by atomic resolution imaging and its quantitative interpretation through simulation. One encounters difficulties in carrying out such experiments owing to the ferromagnetic nature of the majority of phases present in the sample. They introduce drift, astigmatism and other related problems while conducting high resolution imaging experiments. It has been argued in the earlier section 6.3 that the phases might be quite close to each other energetically. As a consequence of this, α-Fe type and Fe_2B_7 phases are mostly found in the ribbon whereas $Fe_{64}Cr_{34}Mo_4$, Fe_5C_2 , and $Fe_{18}Cr_6Mo_5$ phases are observed in ball milled powder and in coating, it is quite possible that other phases might have also nucleated in other regions of the sample locally. As their volume fraction is quite low they are not unambiguously detected in the diffraction pattern and further substantiated by high resolution imaging. It is important to clarify that these phases are primary crystalline phases but not rule out the possibility of having secondary crystalline phases locally [345,371,372]. It is mostly true for all the glass forming alloys and more so for BAS [209,363].

The processing conditions subject the alloy to experience metastability and the possibility of low volume fraction of secondary phase increases [200,355,363]. The nucleation event is statistical in nature and it solely depends on the local environment. In the ball milled powder, local change in structure is observed (cf. Figure 6.6). Even though the structures are related to one another, it is not likely that they have nucleated separately. During ball milling as the energy dissipation varies in different regions of the powder differently, local change in structure is quite likely. In case of nucleation event from the melt, nucleus would always have a tendency to minimize its surface energy. The nucleated nanocrystals are faceted with two different facets forming steps and ledges (cf. Figure 6.8). Difference in atomic density of various planes in the structure controls the surface energy and leading to faceted morphology. However, there are many other factors like local structure of the melt, its chemistry, temperature, diffusivity of the different constituent elements etc., which needs to be taken into account to substantiate as to why these particular facets appear as ledges and steps in comparison to other facets. Owing to the complex nature of chemistry within this structure, it is very difficult to identify the nature of atoms and their numbers present in the advancing planar front. As this information is considered important in the calculation of interfacial energy, the observed structures in the present study are simulated by multislice simulation technique. These multislice simulated images explain that the chemistry of atoms involved in the advancing planar fronts is complex in Fe-Cr-Mo polymorphs compared to other phases. In case of Fe-Cr-Mo phase, the atomic arrangements are getting changed as it transforms to another polymorphic states. In other phases the interaction of surface plane atoms is quite identifiable with the help of multislice simulation as given in the result section 6.3.4 (cf. Figure 6.9).

6.5 Relative thermodynamic stabilities

Relative stability of crystalline and amorphous phases in glass forming alloy system has been assessed successfully before for several other alloy systems [174,175]. As per the above discussion it has been confirmed that the phases that have formed altogether in the powder, ribbon and coating are basically Fe-rich phases. In the powder sample, polymorphs of Fe-Cr-Mo phase along with Fe_5C_2 phase have been observed from the XRD and HRTEM studies. In case of ribbon, α-Fe type and Fe_2B_7 phases have been observed. Whereas in the coating Fe-Cr-Mo phase in its different structural forms have been observed. However, the presence of other phases cannot be ruled out. The important thing here is to determine how much is the relative stability of the multicomponent amorphous matrix with respect to its nanocrystalline phases in each of these three samples. In order to accomplish such a task, the thermodynamics calculations have been done based on the Miedema approach [173]. These calculations have been done for the binary (FeC and FeB) and ternary (FeCrMo) phases [174,175]. Enthalpy versus composition curves as obtained from Miedema calculations have been plotted for FeC and FeB binary systems (cf. Figure 6.16(a-b)).

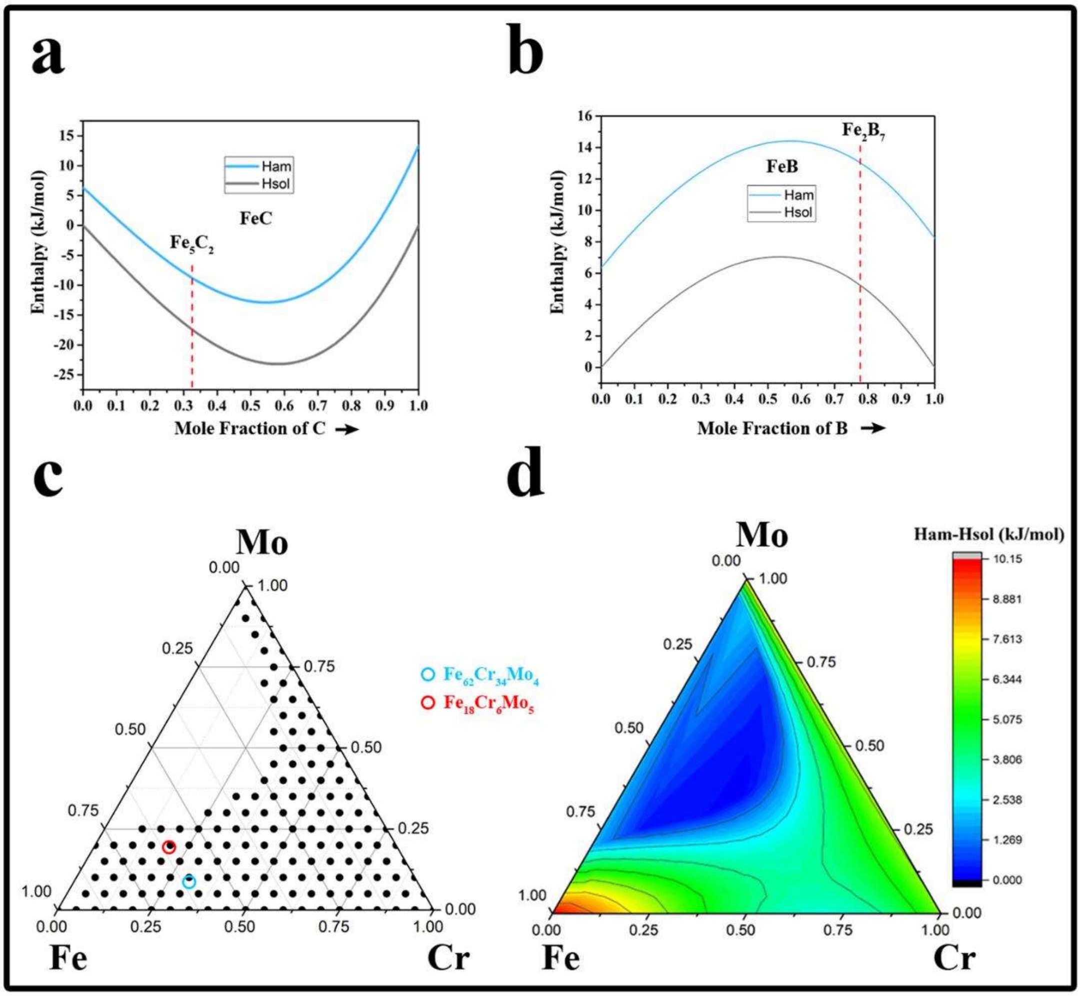

Figure 6.16: ***(a)*** *Enthalpy of formation Vs composition curves for amorphous and crystalline phases of Fe-C system,* ***(b)*** *Enthalpy of formation Vs composition curves for amorphous and crystalline phases of Fe-B system,* ***(c)*** *Ternary plot of Fe-Cr-Mo system in which the empty region represents the glass forming composition region. Open colored circles represent the observed crystalline phase compositions in the amorphous matrix.* ***(d)*** *Ternary contour map of Fe-Cr-Mo system representing the value of enthalpy difference between the amorphous and crystalline phase.*

It is evident from figure 6.16a that the enthalpy of formation for solid solution (crystalline) phase is always less compared to its amorphous phase throughout the composition of Fe-C system. This means that the tendency for the formation of crystalline (FeC) phase is more with respect to its amorphous phase. In addition to this the nature of the curves is concave with minimum enthalpy of formation close to equiatomic composition. This means that the tendency of intermetallics formation is more for this binary system near equiatomic composition. However, in our case the composition of observed Fe_5C_2 phase lies around Fe ~71 at.% and C~ 29 at.% which is marked by dotted (red) line in the figure 6.16a. At this composition the difference in enthalpy of formation between crystalline and amorphous phase has been calculated to be ~ 7.8 kJ/mol. Similarly, for Fe-B system also, the enthalpy of formation for solid solution (crystalline) phase is always less compared to its amorphous phase throughout the composition range as evident from the figure 6.16b. But in this case the nature of curve is convex near the equiatomic composition. This indicates the phase separation tendency of the Fe-B system. This tendency is higher near the equiatomic composition range as enthalpy of formation values for both crystalline and amorphous phase is highly positive within this composition range. However, in our case, the composition of the observed Fe_2B_7 phase lies around Fe ~22 at.% and B ~78 at.% which is marked by dotted (red) line in the figure 6.16b. At this composition, the difference in enthalpy of formation between crystalline and amorphous phase has been calculated to be ~ 7.8 kJ/mol. The information gathered from the above calculations suggest that the relative stability of the amorphous phase coexisting either with Fe_5C_2 phase or with Fe_2B_7 phase is more or less similar. The difference in the value of enthalpy of formation between amorphous and crystalline state in both of these phases is ~ 7.8 kJ/mol.

Now, in order to determine the relative stability of the amorphous phase coexisting either with α-Fe type phase or with the polymorphs of Fe-Cr-Mo phase, Miedema based thermodynamic calculations has been done for the ternary system (FeCrMo). A ternary plot has been constructed based on the relative enthalpy vs composition values as shown in figure 6.16c. The black dots represent such compositions where the enthalpy of formation of crystalline phase is less compared to its amorphous phase. This means that within these composition range (shown by black dots in Figure 6.16c) the relative ease of formation of crystalline phase (FeCrMo) is more. In our case, the compositions of the FeCrMo polymorphs lie within this range as evident from XRD and TEM results. The difference in the value of enthalpy of formation between the amorphous and crystalline phase of ternary system (Fe-Cr-Mo) has been shown in the figure 6.16d as a ternary contour map. The values of enthalpy difference at various compositions in the Fe-Cr-Mo system have been represented as a bar in the same figure with different color codes. It is evident from the XRD and TEM results that the ternary phases of Fe-Cr-Mo system exists as various polymorphs with composition of Fe ~62 at.%, Cr ~34 at.% and Mo ~4 at.% respectively. The value of enthalpy difference between the amorphous and the crystalline state of Fe-Cr-Mo phase at this particular composition is ~7.3 kJ/mol as shown in figure 6.16d. On comparing the value of enthalpy difference in α-Fe type phase and Fe-Cr-Mo phase, it can be suggested that the relative stability of amorphous phase is more when it coexist with α-Fe type phase. This corroborates with our experimental observations of the XRD and TEM results discussed in section 6.3. The XRD results show that the ribbon sample is completely amorphous whereas powder and coating samples display some nanocrystallization along with amorphous phase. It has been shown that the ribbon sample has α-Fe nanocrystals along with Fe_2B_7 nanocrystals in the amorphous matrix (cf. Figure 6.12). In contrast, polymorphs of Fe-Cr-Mo phase are basically in powder and coating samples (cf. Figures 6.4 , 6.5, 6.6 and 6.10). Researchers have shown earlier that the primary crystallizing phase is α-Fe in melt spun ribbons [372]. Moreover, the experimental results and observation comply with the thermodynamic calculations done using the Miedema model. Therefore, this model is found suitable for defining the relative stability of amorphous matrix coexisting with the nanocrystals in each of these samples. It should be further stated that the present alloy compositions lie at the boundary of glass forming composition range. Local composition fluctuation may lead to crystal nucleation locally. The Fe-Cr-Mo composition lies well inside the region where crystalline phase is more stable. It appears that local composition fluctuation leads to nucleation and growth of these phases during processing.

6.6 Conclusions

1. In this study, the three distinct processing routes such as melt-spinning, melt-spinning followed by ball milling and coating on mild steel substrate by thermal spraying technique of $Fe_{58.82}Cr_{11.12}Mo_{1.52}Si_{4.16}B_{15.12}P_{8.88}C_{0.39}$ (at%) alloy evolves different phases. α-Fe and oP30 Fe_2B_7 phases along with the amorphous phase are observed in the melt-spun ribbon. In the melt-spun followed by ball milled powder $Fe_{62}Cr_{34}Mo_4$ phase with oC68, tP60, tP58 structures, $Fe_{18}Cr_6Mo_5$ phase with cI58 structure and Fe_2C_5 Hägg phase with mI32 structure along with the amorphous phase are found. In the coating, $Fe_{18}Cr_6Mo_5$ phase with cF118 and oI92 structures along with amorphous phase are found.
2. The microstructures of the alloy processed through aforesaid three routes are also different. In the melt-spun ribbon α-Fe and Fe_2B_7 nanocrystalline phases are distributed in the amorphous matrix. In the melt-spun followed by ball milled powder Fe-Cr-Mo intermetallic phases with different structures along with Fe_5C_2 Hägg phase and amorphous phases are present, In the coating, faceted and cuboidal nanocrystals of Fe-Cr-Mo intermetallic phase are uniformly distributed in the amorphous matrix.

3. Samples that are melt-spun followed by ball milling display different structures of $Fe_{62}Cr_{34}Mo_4$ intermetallic phases that are derivatives of tP30 structure. Structural changes are manifested in the accommodation of strain energy during the ball milling.
4. Observation of cF118 ($Fe_{18}Cr_6Mo_5$) and oI92 ($Fe_{62}Cr_{34}Mo_4$) phases in the coated sample may further lead to the interpretation that they are derived from the cI58 and tP30 phases respectively by suitably adjusting the lattice parameters and space groups. Such polymorphic transformations are not mechanical energy driven rather they are manifestation of metastable processing conditions.
5. Strain at the interface between two similar polymorphs is owing to tilted domains.
6. Evolution of various phases in three differently processed alloy refers to variable polyhedral coordination environment. The structure of the polyhedra is different from Frank-Kasper polyhedra or Bernal deltahedra. This is a distinctive feature with metal-metal glass forming systems as they are closely related energetically.
7. Calculation of glass forming composition range through Miedema approach shows that the alloy composition lies at the boundary of glass forming composition range. The precipitated phases lie well within the crystalline phase forming range. Local composition fluctuation leads to the nucleation and growth of compositionally different crystalline phases.